Dissertation Submitted in Partial Fulfillment of the Requirements for the Degree of

Doctor of Philosophy

Enhancing Tropospheric Humidity Data Records from Satellite Microwave and Radiosonde Sensors

by

Isaac Moradi

CHALMERS

Department of Earth and Space Sciences
CHALMERS UNIVERSITY OF TECHNOLOGY
Göteborg, Sweden 2015

Enhancing Tropospheric Humidity Data Records from Satellite Microwave and Radiosonde Sensors
ISAAC MORADI
ISBN 978-91-7597-142-1

Doktorsavhandlingar vid Chalmers tekniska högskola
Ny serie nr. 3823
ISSN 0346-718X

Department of Earth and Space Sciences
Chalmers University of Technology
SE–412 96 Göteborg, Sweden
Phone: +46 (0)31–772 1000

Printed in Sweden
Chalmers Reproservice
Göteborg, Sweden 2015

Contact information:
Isaac Moradi
Department of Earth and Space Sciences
Chalmers University of Technology
Hörsalsvägen 9
SE–412 96 Göteborg, Sweden

+46 (0)31–772 1000
+46 (0)31–772 1884
isaacmoradi@gmail.com
www.isaacmoradi.net

Last updated on March 9, 2015.
An up to date version of this thesis will be available on the author's homepage.

Typeset in LaTeX using free open source software.

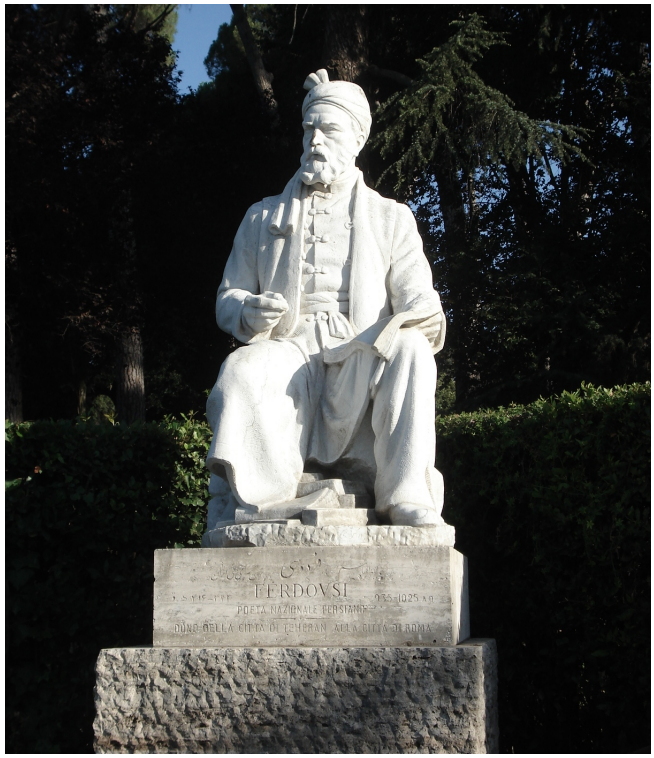

زگهواره تاگوردانش بجوی

Seek knowledge from the cradle to the grave

Persian Poet “Ferdowsi Tusi”, 940–1020 CE

Picture: Statue of Ferdowsi in Rome, Italy (Source: Wikipedia)

Enhancing Tropospheric Humidity Data Records from Satellite Microwave and Radiosonde Sensors

ISAAC MORADI
Department of Earth and Space Sciences
Chalmers University of Technology

Abstract

Water vapor is the most dominant greenhouse gas and plays a critical role in the climate by regulating the Earth's radiation budget and hydrological cycle. A comprehensive dataset is required to describe the temporal and spatial distribution of water vapor, evaluate the performance of climate and weather prediction models in terms of simulating tropospheric humidity, and understand the role of water vapor and its feedback in the climate system. Satellite microwave and radiosonde measurements are two important sources of tropospheric humidity. However, both datasets are subject to errors and uncertainties. The goal of this dissertation was to develop techniques for quantifying and correcting errors in both radiosonde and microwave satellite data. These techniques can be used to homogenize the datasets in order to develop tropospheric humidity climate data records.

The quality of operational radiosonde data were investigated for different sensor types. It was found that the use of a variety of sensors over the globe introduces temporal and spatial errors in the data. Further, it was shown that the daytime radiation dry bias, which is one the most important errors in radiosonde data, depends on both sensor type and radiosonde launch time. The error significantly decreases if daytime data are collected near sunrise or sunset.

Radiometric errors in satellite data were investigated using both inter-comparison of coincident observations as well as validation versus high-quality radiosonde and global positioning system radio occultation data. The results showed that the data from recently launched microwave sounders have a good accuracy relative to each other and simulated data. However, the absolute accuracy of the microwave satellite data can still not be validated due to the lack of reference measurements. In addition, a novel technique for correcting geolocation errors in microwave satellite data was developed based on the difference between ascending and descending observations along the coastlines. Using this method, several important errors including timing errors up to a few hundred milliseconds, and sensor mounting errors up to 1.2° were found in some of the microwave instruments.

Finally, since satellite data are indirect measurements, a method was developed to transform satellite radiances from different water vapor channels to layer averaged humidity. The technique is very fast because radiative transfer calculations are only required to determine the empirical coefficients.

Keywords: remote sensing, water vapor, microwave, radiosonde, climate, CDR, homogenization, radio-frequency, antenna, humidity, troposphere, meteorology

List of Publications

Appended Papers

List of publications that are included in the dissertation.

Paper I

I. Moradi, S. Buehler, V. John, and S. Eliasson, **Comparing upper tropospheric humidity data from microwave satellite instruments and tropical radiosondes**, *Journal of Geophysical Research: Atmospheres*, 115(D24), p. D24310, 2010

Paper II

I. Moradi, H. Meng, and R. Ferraro, **Correcting geolocation errors for microwave instruments aboard NOAA satellites**, *Geoscience and Remote Sensing, IEEE Transactions on*, 51(6), p. 3625 – 3637, 2013

Paper III

I. Moradi, B. Soden, R. Ferraro, Ph. Arkin, and H. Vomel, **Assessing the quality of humidity measurements from global operational radiosonde sensors**, *Journal of Geophysical Research: Atmospheres*, 118(14), p. 8040–8053, 2013

Paper IV

I. Moradi, R. Ferraro, B. Soden, P. Eriksson, and Ph. Arkin, **Retrieving layer averaged tropospheric humidity from Advanced Technology Microwave Sounder (ATMS) water vapor channels**, *Geoscience and Remote Sensing, IEEE Transactions on*, revised, 2015

Paper V

I. Moradi, R. Ferraro, P. Eriksson, and F. Weng, **Inter-calibration and validation of observations from ATMS and SAPHIR microwave sounders**, *Geoscience and Remote Sensing, IEEE Transactions on*, revised, 2015

Related Papers

List of papers that were published as a part of the research but are not included in the dissertation.

Paper VI

I. Moradi and R. Ferraro, 2014. **Inter-calibration of microwave satellite data: an ongoing challenge**, *Global Space-based Inter-Calibration System (GSICS) Quarterly, Special Issue on Microwave*, Vol 8, doi: 10.7289/V55H7D64 (leading paper of the special issue)

Paper VII

I. Moradi and R. Ferraro, 2014. **Inter-calibration of observations from SAPHIR and ATMS instruments**, *Global Space-based Inter-Calibration System (GSICS) Quarterly, Special Issue on Microwave*, Vol 8, doi: 10.7289/V55H7D64

Paper VIII

I. Moradi, S. Buehler, V. John, T. Reale, and R. Ferraro, 2013. **Evaluating instrumental inhomogeneities in global radiosonde upper tropospheric humidity data using microwave satellite data**, *Geoscience and Remote Sensing, IEEE Transactions on*, 51(6), pp. 3615–3624, doi: 10.1109/TGRS.2012.2220551

Paper IX

I. Moradi, S. Buehler, V. John, 2010. **Comparing upper tropospheric humidity from microwave satellite instruments and IGRA radiosonde data**, *Microwave Radiometry and Remote Sensing of the Environment (MicroRad), 2010 11th Specialist Meeting on*, 51(6), pp. 146–151, doi: 10.1109/MICRORAD.2010.5559573

Acknowledgments

I would like to express my special thanks to my supervisor, Professor Patrick Eriksson, for his enthusiasm, patience, and the encouragement he provided throughout this dissertation. Many thanks to my co-supervisor, Professor Brian Soden, for sharing his immense knowledge and also for his excellent feedback on the papers. Special thanks to the Deputy Head of the Department of Earth and Space Sciences, Professor Donal Murtagh, for supporting me for the dissertation and also for the course work. Many thanks to the administrative staff at the Department of Earth and Space Sciences for practical support throughout my PhD dissertation, including Paulina Sjögren and Marita Nelin.

I am grateful to my colleagues at the University of Maryland and NOAA, especially Mr. Ralph Ferraro, Dr. Hugo Berbery, Dr. Phillip Arkin, Professor Antonio Busalacchi and all ESSIC administrative staff for their support since I moved to the States. Two of the papers, appended to the dissertation, were from the research funded by NOAA through Cooperative Institute for Climate and Satellites (CICS-MD).

Part of this Ph.D. dissertation was carried out at the Department of Computer Science, Electrical and Space Engineering, Lulea Technical University and Swedish National Graduate School of Space Technology. Special thanks goes to all colleagues and countless friends who helped while up there in Kiruna.

I would like to express my heartiest appreciation to my beloved wife who spent sleepless nights all these years taking care of my beautiful sons, Arian and Armin. She was always my support in the moments when there was no one to help. This dissertation is dedicated to her. Last but not least, words cannot express how thankful I am to my mother and my father for their love and support throughout my life.

Credits & About

This dissertation was written in LaTeX, using latex templates made by Markus Billeter and Ludde Edgren. Billeter's template was originally created by Fredrik Warg and updated by Martin Thuresson, for more information see
http://www.cse.chalmers.se/~billeter.

The document also uses 'ccBeamer 0.1' by Sebastian Pipping, which is licensed under Creative Commons Attribution–ShareAlike 3.0, available at
http://blog.hartwork.org/?p=52

Table of Contents

Acronyms

AMSU-A Advanced Microwave Sounding Unit-A 6, 32, 35–39, 44, 61

AMSU-B Advanced Microwave Sounding Unit-B 6, 21, 32, 35, 37–39, 44, 60, 61

ARM Atmospheric Radiation Measurement 6, 54, 55, 57, 59–61, 64

ATMS Advanced Technology Microwave Sounder 6, 8, 9, 18, 25, 26, 35, 39–42, 44, 59, 63, 64

CDR Climate Data Record 6, 59–61, 64

ECMWF European Center for Medium range Weather Forecasting 63

ESDR Earth System Data Record 6, 59

GPS-RO Global Positioning System - Radio Occultation 59, 63

GRUAN GCOS Reference Upper Air Network 54, 64

IGRA Integrated Global Radiosonde Archive 6, 54–57

IPCC Intergovernmental Panel on Climate Change 5

LTE Local Thermodynamic Equilibrium 12, 15

M-T Megha-Tropiques 40, 63, 65

MADRAS Microwave Analysis and Detection of Rain and Atmospheric Systems 40

MHS Microwave Humidity Sounder 6, 35, 37–39, 44, 60, 61

NCDC NOAA's National Climatic Data Center 55, 62

NOAA National Oceanic and Atmospheric Administration 49

NWP Numerical Weather Prediction 60, 61

RTE Radiative Transfer Equation 11, 15, 17, 22, 23

RTM Radiative Transfer Modelling 11, 20

S-NPP Suomi National Polar-orbiting Partnership 39, 63

SAPHIR Sondeur Atmospherique du Profil d' Humidité Intropicale par Radiométrie 6, 25, 26, 35, 40–42, 59, 63, 64

UTH Upper Tropospheric Humidity 8, 60, 61

WMO World Meteorological Organization 56

Part I

Principles & Theory

"Each ray of light moves in the coordinate system 'at rest' with the definite, constant velocity V independent of whether this ray of light is emitted by a body at rest or a body in motion."

Albert Einstein

1

Introduction and Overview

Atmospheric water vapor is mainly produced by evaporation from oceans, inland waters, wet land surfaces, and evapotranspiration from plants. Water vapor forms only a small portion of the Earth's atmosphere, but still has a significant impact on the Earth's climate.

1.1 Water Vapor Terminology

The atmospheric water vapor content can be expressed in several different ways. The most common ways, i.e., absolute humidity, specific humidity, relative humidity, and mixing ratio, are presented in this section. For more information the reader is referred to Ahrens (2007, Chapter 4) and Rogers and Yau (1989).

Absolute humidity (ϱ) indicates the density of water vapor in the air and is calculated as the ratio of the mass of water vapor (m_w) to the total volume of the air (v_a):

$$\varrho = \frac{m_w}{v_a} \tag{1.1}$$

Atmospheric water vapor behaves as an ideal gas to a good approximation. Therefore, the equation of state for water vapor can be expressed as:

$$e = \varrho R_v T \tag{1.2}$$

where e is the water vapor pressure in Pa, R_v is the specific gas constant for water vapor ($461.5\,\mathrm{J\,kg^{-1}\,K^{-1}}$), T is temperature in K, and absolute humidity (ϱ) is in $\mathrm{kg\,m^{-3}}$ (Rogers and Yau, 1989). Thus, the absolute humidity can be calculated using the vapor pressure and temperature as:

$$\varrho = \frac{e}{R_v T} \tag{1.3}$$

Specific humidity (q) is the ratio of the mass of water vapor (m_w) to the mass of the moist air:

$$q = \frac{m_w}{m_d + m_w} \tag{1.4}$$

where m_d is the mass of dry air, and $m_d + m_w$ is the total mass of the moist air. Similarly, mass mixing ratio (r) is defined as the mass of water vapor (m_w) to the mass of dry air and can be calculated using water vapor pressure (e) and air pressure (p) as follows:

$$r = \frac{m_w}{m_d} = \frac{\varrho}{\rho_d} = \varepsilon \frac{e}{p - e} \tag{1.5}$$

where ρ_d is the density of dry air, ε is the ratio of the specific gas constant of dry air ($R_d = 287.058\,\mathrm{J\,kg^{-1}\,K^{-1}}$) to the specific gas constant of water vapor (R_v) and is equal to 0.622. By combining Equations 1.4 and 1.5, specific humidity can be calculated from either mass mixing ratio or vapor pressure as follows:

$$q = \frac{r}{1 + r} = \varepsilon \frac{e}{p} \tag{1.6}$$

Volume mixing ratio (r') is the ratio of the number of moles of water vapor (n_w) to the number of moles of dry air (n_d) and can be calculated from mass mixing ratio (r) as follows:

$$\left.\begin{aligned} r &= \frac{n_w M_w}{n_d M_d} \\ r' &= \frac{n_w}{n_d} \end{aligned}\right\} \implies r' = r \frac{M_d}{M_w} = \frac{1}{\varepsilon} r \tag{1.7}$$

where M_w is the molar mass of water ($18.016\,\mathrm{gr\,mol^{-1}}$), and M_d is the molar mass of dry air ($28.966\,\mathrm{gr\,mol^{-1}}$).

Due to the low concentration of water vapor in the air, especially at high altitudes, parts-per million (ppm) is sometimes used to express the concentration of water vapor in the air. One ppm is defined as moles of water vapor to million moles of the air (ppm_v) which is equal to $r' \times 10^6$. In addition, ppm can also be defined as milligrams (mg) of water vapor per one kilogram (kg) of dry air which is equal to $r \times 10^6$.

Relative humidity (RH) is the ratio of the amount of water vapor in the air to the amount of water vapor when the air is saturated. Relative humidity can

Table 1.1: *Coefficients for saturation water vapor equation.*

Coef.	$T > 0$	$T < 0$
K_0	$-0.604\,361\,17 \times 10^4$	$-0.586\,536\,96 \times 10^4$
K_1	$0.189\,318\,833 \times 10^2$	$0.222\,410\,330\,0 \times 10^2$
K_2	$-0.282\,385\,94 \times 10^{-1}$	$0.137\,490\,42 \times 10^{-1}$
K_3	$0.172\,411\,29 \times 10^{-4}$	$-0.340\,317\,75 \times 10^{-4}$
K_4	0	$0.269\,676\,87 \times 10^{-7}$
K_5	$0.285\,848\,7 \times 10^1$	$0.691\,865\,1$

be calculated as either the ratio of the actual water vapor pressure (e) to the saturation water vapor pressure (e_s) or the ratio of actual mixing ratio (r) to the saturation mixing ratio (r_s) as follows:

$$RH = \frac{e}{e_s} = \frac{r}{r_s} \tag{1.8}$$

The saturation mixing ratio (r_s) can be calculated using Equation 1.5 by replacing e with e_s. The saturation water vapor pressure (e_s) over liquid can be calculated as follows (Wexler, 1976, 1977):

$$\ln(e_s) = \sum_{j=0}^{4} K_j T^{j-1} + K_5 \ln(T) \tag{1.9}$$

where T is temperature in K, and K_0 to K_5 are given in Table 1.1 separately for temperatures greater than 0 °C (Wexler, 1976) and lower than 0 °C (Wexler, 1977).

Humidity measurements are normally available in either water vapor pressure, relative humidity, or dew point. Dew point is the temperature at which the water vapor of the air is saturated and can be converted to water vapor pressure using Equation 1.9.

1.2 Water Vapor in the Climate System

Water vapor is the most abundant of the natural greenhouse gases in the atmosphere and influences the Earth's climate and radiation budget, because of its greenhouse effect. It affects the water and hydrologic cycle, through evaporation, condensation, and precipitation. Water vapor also drives the extreme weathers such as rainstorms and floods. The initiation and evolution of convective storms are also strongly affected by the amount and distribution of middle to lower tropospheric water vapor (Keil et al., 2008). The latent heat of water vapor is responsible for nearly half of the poleward and most of the upward

heat transfer (Sherwood et al., 2010). In addition, the layer above the planetary boundary layer often knows as free troposphere, approximately above 1-2 km, strongly contributes to the water vapor feedback through latent heat and radiation processes (Dessler and Sherwood, 2009; Held and Soden, 2006; Trenberth et al., 2009).

Water vapor enhances the sensitivity of the climate to external forcings by about 70%, thus playing an important role in global warming and climate change predictions (Cess et al., 1990). For instance, in the climate models an approximately constant relative humidity doubles the temperature rise relative to when the water vapor feedback is forced to be zero (Minschwaner and Dessler, 2004; Soden et al., 2005). However, the total radiative effect of water vapor depends on the strength of the other feedbacks in the climate system (Held and Soden, 2000).

It should be noted that in addition to specific humidity, relative humidity is also of great importance in the climate system, because some atmospheric processes, e.g., radiative effects, can be more easily described in terms of relative humidity (Sherwood et al., 2010). Studies have shown that relative humidity and vapor mixing ratios have a non-Gaussian distribution, meaning that the water vapor equilibria are not controlled by random processes (Sherwood et al., 2006). However, relative humidity is estimated to stay fairly stable under climate change in the planetary boundary layer, at least over ocean, because any significant change in relative humidity causes dramatic changes in evaporation (Betts and Ridgway, 1988). However, factors that control relative humidity in free troposphere are not well known (Pierrehumbert et al., 2007), thus the relation between increase in humidity and temperature in the free troposphere may not be as strong as their relation in the planetary boundary layer (Sherwood, 2010).

1.3 Water Vapor and Global Warming

The greenhouse effect was first discovered by Joseph Fourier in 1827. In 1861, John Tyndal discovered that the gases dominating the greenhouse effect are carbon dioxide and water vapor, despite their low mixing ratio in the atmosphere. The major atmospheric constituents, i.e., nitrogen, oxygen, and argon, are not affected by infrared radiation, thus do not contribute to the greenhouse effect. The wavelength-dependence of the absorption was discovered in early 20th century after the development of quantum theory as well as improvement in spectroscopy measurements (Held and Soden, 2000).

Although it is expected that the relative humidity remains (nearly) constant at all levels, the overall picture is that the fractional increase in upper tropospheric water vapor, e.g., fractional increase in specific amount of humidity, or volume mixing ratio, will be roughly three times as large as that in the lower troposphere (Soden et al., 2005). This large increase in upper tropospheric water vapor is first due to the relation between saturation vapor pressure and temperature as described by the Clausius-Clapeyron equation:

$$\frac{\mathrm{d}e_s}{\mathrm{d}T} = \frac{L_\nu\,(T)\,e_s}{R_\nu T^2} \tag{1.10}$$

where e_s is the saturation vapor pressure, T is the temperature, and L_ν is the specific latent heat of evaporation ($2.26 \times 10^6\,\mathrm{J\,kg^{-1}}$). Equation 1.10 shows that fractional increase in e_s scales according to $\frac{\mathrm{d}e_s}{e_s} \propto \frac{\mathrm{d}T}{T^2}$. Thus, under constant relative humidity, the fractional change in vapor pressure resulting from a 1 K warming at $T_1 = 200$ K will be more than twice than that obtained at $T_2 = 300$ K, the ratio is equal to T_2^2/T_1^2. The second reason for the large increase in the upper troposphere humidity is that most climate models predict a reduction in lapse-rate with increasing surface temperature. Thus the upper troposphere tends to warm more than the lower troposphere, further amplifying the upper tropospheric moistening (Held and Soden, 2000; Minschwaner and Dessler, 2004; Soden et al., 2005).

There is also a regional dependency for the water vapor feedback that depends on the way water vapor is assumed to be perturbed. For instance, one can assume equal fractional perturbations in either vapor pressure, mixing ratio (Shine and Sinha, 1991), or relative humidity (Spencer and Braswell, 1997). Thus, it is essential to understand not only the temporal distribution of water vapor, but also to understand the spatial distribution of water vapor and the physical processes that control the distribution of water vapor (Chung et al., 2011).

In 1990, the Intergovernmental Panel on Climate Change (IPCC) reported that the water vapor feedback is the best understood mechanism feedback in the climate system. However, IPCC amended this perspective in 1995, and reported that uncertainty due to redistribution of water vapor remains the biggest source of uncertainty in the climate models (Held and Soden, 2000).

All the climate models show a strong water vapor feedback, but the magnitude of this feedback differs among the models (Dessler and Sherwood, 2009; Held and Soden, 2000), mainly because of differences in the amount of upper tropospheric warming among the climate models. However, the difference in the amount of water vapor feedback in global climate models is largely compensated by the lapse-rate feedback, a negative feedback with an opposite spread (Dessler and Sherwood, 2009). It is generally accepted that the water vapor feedback is positive with a magnitude of $1.5\,\mathrm{W\,m^{-2}/K}$ to $2\,\mathrm{W\,m^{-2}/K}$ (Dessler and Sherwood, 2009). The feedback is also estimated to be relatively larger in the tropical region (Held and Soden, 2000). As mentioned, this magnitude of feedback will roughly double the global warming (Dessler and Sherwood, 2009).

The uncertainties in projecting the water vapor feedback arise from different sources, including uncertainty in the water vapor continuum that is used by climate and weather prediction models to conduct the radiative transfer calculations. However, the errors in the continuums are not significant enough to limit our understanding of the climate sensitivity (Held and Soden, 2000). Another

source of uncertainty is the lack of reliable water vapor measurements to evaluate the performance of climate models (Held and Soden, 2000; Sherwood et al., 2010). The errors in the observations are especially a limiting factor for evaluating the performance of climate models in terms of simulating free tropospheric humidity (Chung et al., 2011; Sherwood et al., 2006).

In summary, despite the importance of water vapor in the climate system, there is a considerable uncertainty in our knowledge of the distribution of tropospheric humidity and the processes controlling it. The research efforts have not yet been able to clearly describe the intensity of the water vapor feedback in the atmosphere, factors influencing the amount of water vapor, and even the concentration of water vapor in many regions of the atmosphere, and as yet, no accepted knowledge exists about the trend of water vapor (Sherwood et al., 2010). Although most available observations show an upward trend, inhomogeneity in the data, length of observational records, and differences among the observed trends, restrict us from establishing a clear picture of the trend in water vapor and its climate feedback (Sherwood et al., 2010) A comprehensive dataset is required to understand the role of atmospheric humidity in the Earth's climate system and also to evaluate the climate models (Held and Soden, 2000). In addition to the temporal distribution of water vapor, the spatial distribution of water vapor is also of great importance for understanding the moisture transport and earth energy budget (Randel et al., 1996).

1.4 Water Vapor Measurements

Two important data sources for retrieving tropospheric humidity are in-situ radiosonde and spaceborne observations. In this research, we used radiosonde data from the Atmospheric Radiation Measurement (ARM) and the Integrated Global Radiosonde Archive (IGRA), and satellite data from the Advanced Microwave Sounding Unit-A (AMSU-A), the Advanced Microwave Sounding Unit-B (AMSU-B), the Microwave Humidity Sounder (MHS), the Advanced Technology Microwave Sounder (ATMS), and Sondeur Atmospherique du Profil d' Humidité Intropicale par Radiométrie (SAPHIR). Both radiosonde and satellite observations are subject to errors and uncertainties and do not yet meet the requirements for long-term climate assessments. In recent years, much attention has been given to developing long-term homogenized and bias-corrected data records from satellite and in-situ observations. These long-term homogenized and bias corrected data records are known as Earth System Data Record (ESDR) or Climate Data Record (CDR). National Research Council (U.S.) (2004) defines a ESDR/CDR as "a time series of measurements of sufficient length, consistency, and continuity to determine climate variability and change".

Microwave Satellite Data

Satellite data provide global coverage and are available from both microwave and infrared sensors. Infrared observations are available for a longer time pe-

riod, but microwave observations are less sensitive to clouds, therefore provide opportunity to develop a dataset in almost all-weather conditions. Continuous measurements of mid-upper tropospheric relative humidity are available since 1979 from infrared instruments and since 1987 from microwave instruments.

Satellite data are subject to several errors that can be classified into radiometric and geometric errors. Radiometric errors are caused by several factors such as drift in sensor calibration, Radio Frequency Interference (RFI), uncertainty in the temperatures of warm and cold (space-view) targets, and non-linearity in the calibration. Due to the lack of reference measurements identical to microwave satellite data (i.e., same geometry and same physical quantity), alternative methods, such as inter-comparing coincident observations from similar instruments, and validation versus simulated observations using a radiative transfer model, are employed to quantify and correct the radiometric errors. The temperature and humidity profiles from radiosonde and reanalyses can be used as input for the radiative transfer calculations.

Inter-calibrating similar spaceborne instruments is especially useful for generating long-term data records. In this case, one of the instruments that does not have orbital or calibration drift over time is considered as the reference instrument. Observations from the other instruments (target instruments) are inter-calibrated with respect to the reference instrument. In some cases, it is not possible to directly compare the reference and target instruments because of either small frequency difference between the channels or difference in the geometry of the instruments. In this case, a third instrument or simulated observations using radiative transfer calculations are used to transfer the calibration from the reference instrument to the target instruments. The difference between the reference and target instrument is calculated as $\Delta D = D_1 - D_2$, where D_1 is the difference between reference and third instrument, and D_2 is the difference between target and third instrument, and ΔD is knows as double difference or the difference between differences.

Geolocation error is another important source of uncertainty in microwave satellite data. Geolocation errors are caused by several factors such as sensor misalignment, satellite clock offset, and sensor modeling errors. Geolocation of microwave satellite data can not be easily validated using coastline checks because of the coarse spatial resolution of microwave observations. Therefore, advanced techniques are required to quantify the geolocation errors in microwave satellite data.

Radiosonde Data

In-situ radiosonde observations provide direct measurement of vertical profiles of tropospheric water vapor and are available for a longer time-period than satellite data. However, radiosonde data are only available from around 1500 upper-air stations with a non-uniform global distribution. Radiosonde humidity sensors and measured data are subject to several errors, particularly in the dry

and cold conditions of the middle to upper troposphere. Some of these errors include contamination, sensor design, calibration, and data processing (Elliott and Gaffen, 1991; Miloshevich et al., 2001; Moradi et al., 2013). Below a brief description of the quality control of the radiosonde data is provided, but the errors and uncertainties are discussed in more detail in Chapter 4.

One of the conventional methods for evaluating the accuracy of radiosonde senors and measurements is comparing the measurements from the target sensor with measurements from a reference sensor attached to the same balloon. This method has been used in many inter-comparison campaigns and ensures that both sensors sample the same air. This method is suitable for quantifying the errors in individual radiosonde sensors but it cannot be used globally since it is expensive and time consuming. Besides, some of the errors in radiosonde measurements are due to operational practices rather than the radiosonde sensors. Thus, measurements from the same sensor type may have different accuracy at different stations. Because of these limitations, evaluating the quality of radiosonde data from global operational radiosonde networks has always been a challenge. In the lack of reference datasets to evaluate the quality of global radiosonde data, alternative methods such as comparing data from neighboring stations, and also comparison with independent datasets such as satellite data have been employed. The former, comparison with data from neighboring stations, can be misleading if both stations utilize similar sensors which may have similar biases.

Satellite data from microwave sensors have global coverage and provide a valuable dataset for quantifying the accuracy of operational radiosonde data. However, microwave satellite data first need to be bias corrected and validated to be able to serve as the reference dataset. In addition, because of temporal and spatial mismatch between radiosonde and satellite data, appropriate filters are required to ensure that the coincident observations from radiosondes and satellites represent the same air sample. Satellite data are layer-averaged while radiosonde data provide vertical profiles of tropospheric water vapor, therefore the two datasets cannot be directly compared. It is required to either derive the atmospheric water vapor profiles from satellite data using inversion techniques, or simulate satellite data from radiosonde profiles and a radiative transfer model. Both methods depend on radiative transfer calculations, but it is generally less challenging to simulate satellite radiances from the radiosonde profiles.

1.5 Radiance to Humidity Transformation

Microwave satellite data are indirect measurements of atmospheric parameters, while in most cases, geophysical variables, such as water vapor, are required for scientific research. Therefore, transformation techniques are required to derive geophysical variables from satellite observations. These techniques can be classified into inversion and direct transformation methods. The inversion methods normally require computationally expensive calculations and a-priori informa-

tion to derive the posterior information. Microwave instruments suitable for retrieving water vapor normally offer a few channels near the water vapor absorption line at 183 GHz. The weighting functions of these channels are very broad, inter-correlated, and do not completely cover the entire troposphere. Therefore, the inversion problems are severely under-determined for the current microwave humidity observations.

A simple transformation technique was first introduced by Soden and Bretherton (1993) to directly transform satellite observations from infrared sensors into Upper Tropospheric Humidity (UTH). The technique was later modified by Spencer and Braswell (1997) and Buehler and John (2005) to derive UTH from microwave satellite data. This technique was extended to the ATMS water vapor channels as a part of this dissertation to derive upper to lower-tropospheric humidity from ATMS observations. The transformation technique relates natural logarithm of layer-averaged relative humidity (LAH) with satellite measurements as follows:

$$\ln(LAH) = a + bTb \tag{1.11}$$

where ln is the natural logarithm, a and b are the empirical coefficients to be determined, and Tb is the observed brightness temperature in Kelvin, see Equation 2.7 for the definition of brightness temperature. Figure 1.1 shows an example of the relation between layer-averaged tropospheric humidity and brightness temperatures of the ATMS Channel 183±7 GHz.

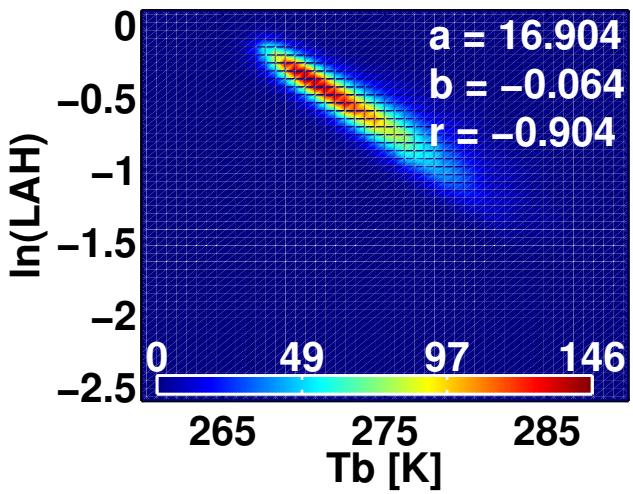

Figure 1.1: *Relation between layer averaged tropospheric humidity and brightness temperatures of ATMS Channel 183±7 GHz. Colorbar shows number of datapoints, the a and b values are the offset and slope of the fitted line (see Equation 1.11), and r is the correlation coefficient between Tb and* $\ln(LAH)$.

1.6 Objectives and Structure

This summary provides an overview and some technical background that are required to understand the published (and related) papers. The aim is not to provide a comprehensive technical discussion, but only to provide a general description of the theory and the technical terms that are commonly used in satellite microwave remote sensing, radiative transfer modeling, and in-situ radiosonde measurements. Chapter 1 gives an introduction to the importance of water vapor in the climate system and also briefly describes the satellite microwave and radiosonde measurements of tropospheric water vapor, Chapter 2 introduces radiative transfer modeling and related concepts, Chapter 3 describes different technical terms that are often used in microwave remote sensing, Chapter 4 introduces radiosonde measurements and explains some of the major errors and uncertainties in radiosonde observations, and Chapter 5 summarizes this dissertation, provides a list of papers published as a part of the dissertation, and gives an outlook for future work.

2

Microwave Radiative Transfer Modeling

Radiative transfer is the transfer of energy in the form of electromagnetic radiation. The Radiative Transfer Equation (RTE) explains how much of the propagated radiation will be absorbed, scattered, or transmitted while passing through the atmosphere. In atmospheric remote sensing, Radiative Transfer Modelling (RTM) simulates the propagation of electromagnetic radiation through the Earth's atmosphere. Because of the importance of RTM in atmospheric remote sensing, this chapter briefly introduces some fundamentals of RTM, including physical laws related to black body radiation, electromagnetic theory, and radiation laws. In addition, radiative transfer calculations for passive microwave instruments detecting incoherent radiation are discussed.

2.1 Radiation Laws

One of the fundamental concepts in RTM is an idealized object called *black body* that absorbs all the incident radiation independent of frequency (Siegel, 2001, Chapter 1). Plank's law describes the intensity of radiation emitted by a black body as a function of temperature and frequency or wavelength:

$$B_\nu(T) = \frac{2h\nu^3}{c^2\left(e^{h\nu/kT} - 1\right)} \tag{2.1}$$

$$B_\lambda(T) = \frac{2hc^2}{\lambda^5\left(e^{hc/\lambda kT} - 1\right)} \tag{2.2}$$

where T is absolute temperature in Kelvin, ν is frequency in Hz, λ is wavelength in meter, k is the Boltzmann constant ($1.380\,648\,8 \times 10^{-23}\,\mathrm{J\,K^{-1}}$), h is the Planck constant ($6.626\,069\,57 \times 10^{-34}\,\mathrm{J\,s^{-1}}$), and c is the speed of the light ($299\,792\,458\,\mathrm{m\,s^{-1}}$) (Kaviany, 2001, Chapter 4). Equation 2.1 gives a black body's radiation per unit frequency and has the unit of $\mathrm{W\,sr^{-1}\,m^{-2}\,Hz^{-1}}$, while Equation 2.2 gives a black body's radiation per unit wavelength and has the unit of $\mathrm{W\,sr^{-1}\,m^{-2}\,m^{-1}}$. The black body radiation within any given spectral band must be the same regardless of formula (Sharkov, 2003, Chapter 6):

$$B_\nu \mathrm{d}\nu = B_\lambda \mathrm{d}\lambda \implies B_\lambda = \frac{\nu^2}{c} B_\nu = \frac{c}{\lambda^2} B_\nu \tag{2.3}$$

In Planck's law, $h\nu$ is the energy of a photon and kT is the ambient thermal energy. In the low energy limit, such as the microwave region, $h\nu \ll kT$ and the exponential in Equations 2.1 and 2.2 can be expanded in a Taylor series. In that case, Planck's law is simplified to a linear relation between radiation and temperature, which is known as Rayleigh-Jeans approximation (Siegel, 2001, Chapter 1):

$$B_\nu(T) = \frac{2\nu^2 kT}{c^2} \tag{2.4}$$

$$B_\lambda(T) = \frac{2ckT}{\lambda^4} \tag{2.5}$$

Black bodies absorb all incident radiation, so do not transmit or reflect radiation, but many terrestrial objects also reflect or transmit the incident radiation. Therefore, these objects cannot be considered as a black body and are often referred to as a *gray body*. The behavior of gray bodies can still be described using the black body concept, but the amount of radiation that is emitted or absorbed by these objects is rated by emissivity (ε_v) which is defined as follows:

$$\varepsilon_v = \frac{I_\nu}{B_\nu(T)} \tag{2.6}$$

where I_ν is the radiation emitted by the gray body (Kaviany, 2001, Chapter 4). Equation 2.6 shows that the radiation emitted by a surface can be calculated as $\varepsilon_v B_\nu(T)$. Furthermore, according to Kirchhoff's law, in Local Thermodynamic Equilibrium (LTE), the absorption and emission coefficients are always equal (Goody and Yung, 1989, Chapter 2).

2.2 Brightness Temperature

Brightness Temperature (Tb) is the temperature of a black body in LTE that duplicates the intensity of a grey body at a given frequency. Brightness temper-

ature can be calculated using the inverse of Planck function for a given intensity at a given frequency as follows:

$$Tb = \frac{h\nu}{k} \ln^{-1}\left(1 + \frac{2h\nu^3}{I_\nu c^2}\right) \tag{2.7}$$

Brightness temperature can also be calculated using the inverse of Rayleigh-Jeans approximation, but it should be noted that the Rayleigh–Jeans approximation is not accurate for very low temperatures (Hewison and Saunders, 1996; Janssen, 1993; Weng and Zou, 2013).

2.3 Radiance and Flux

Spectral monochromatic radiation intensity (I_ν), also referred to as spectral intensity or spectral radiance, describes the amount of radiant energy ($\mathrm{d}E$) transferred in a given direction ($\mathbf{\Omega}$), per unit cross sectional area perpendicular to the propagation direction, per unit time ($\mathrm{d}t$), per unit solid angle ($\mathrm{d}\Omega$), and per unit frequency ($\mathrm{d}\nu$):

$$\mathrm{d}I_\nu\left(\mathbf{r}, \mathbf{\Omega}, t\right) = \frac{\mathrm{d}E_\nu}{\mathrm{d}A\cos\theta\,\mathrm{d}\Omega\,\mathrm{d}\nu\,\mathrm{d}t} \tag{2.8}$$

where $\mathrm{d}A\cos\theta$ is the projection of $\mathrm{d}A$ on the plane perpendicular to the propagation direction, $\mathbf{r}$ is the spatial coordinate of $\mathrm{d}A$, θ is the angle between normal to the surface ($\mathbf{n}$) and propagation direction ($\mathbf{\Omega}$). The unit of spectral intensity is thus $\mathrm{W\,sr^{-1}\,m^{-2}\,Hz^{-1}}$ (Liou, 2002; Sharkov, 2003). If the intensity does not depend on the direction, then the field is denoted as isotropic.

Solid angle is a two dimensional angle in three dimensional space and corresponds to the fraction of the surface of a sphere that is covered by the projection of a particular object on the sphere, see Figure 2.1. Solid angle is dimensionless and is expressed in the unit of steradian (sr). Solid angle is calculated using the cross-section of the object projected on the sphere (A) and the radius of the sphere (r) as follows:

$$\Omega = \frac{A}{r^2} = \int_\phi\int_\theta \sin\theta\,\mathrm{d}\theta\,\mathrm{d}\phi \tag{2.9}$$

where ϕ indicates the azimuth angle.

The intensity of radiation emitted by an elementary surface area or falling on it within a specific solid angle ($\hat{I}_\nu$) is determined as follows:

$$\hat{I}_\nu = \int_{\phi 1}^{\phi 2}\int_{\theta 1}^{\theta 2} I_\nu(\mathbf{r}, \mathbf{\Omega}, t)\cos\theta\sin\theta\,\mathrm{d}\theta\,\mathrm{d}\phi \tag{2.10}$$

where $\sin\theta\,\mathrm{d}\theta\,\mathrm{d}\phi$ indicates the elementary solid angle ($\mathrm{d}\Omega$) in polar coordinates (Sharkov, 2003, Chapter 5).

Flux or irradiance is the intensity integrated over the entire spherical solid angle. The upwelling $F_\nu\uparrow$ and downwelling $F_\nu\downarrow$ atmospheric fluxes can be calculated as follows (Thomas and Stamnes, 2002, Chapter 2):

$$\begin{aligned} F_\nu\uparrow &= \int_{\phi=0}^{2\pi}\int_{\theta=0}^{\pi/2} I_\nu\uparrow(\theta,\phi)\cos\theta\,\sin\theta\,\mathrm{d}\theta\,\mathrm{d}\phi \\ F_\nu\downarrow &= -\int_{\phi=0}^{2\pi}\int_{\theta=\pi/2}^{-\pi} I_\nu\downarrow(\theta,\phi)\cos\theta\,\sin\theta\,\mathrm{d}\theta\,\mathrm{d}\phi \end{aligned} \tag{2.11}$$

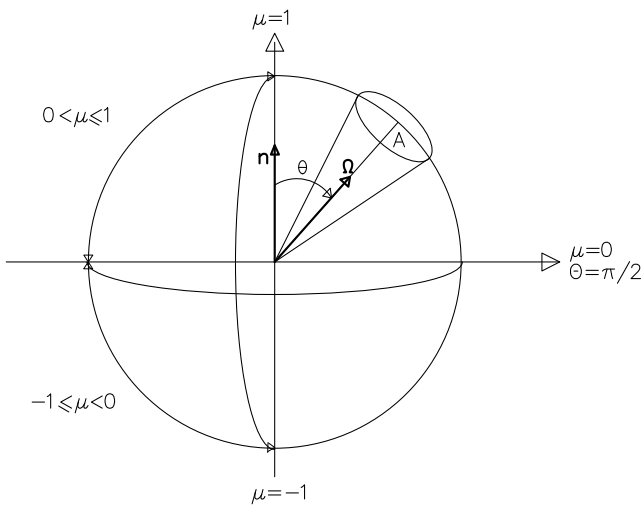

Figure 2.1: *The concept of solid angle related to the incidence angle, and the direction of propagation.*

2.4 Radiative Transfer Equation

The equation of radiative transfer describes the amount of radiation that is lost due to absorption, added due to emission, or redistributed due to scattering. The attenuation of radiation in an absorbing medium ($\mathrm{d}I_\nu$) depends on the intensity of the incident radiation (I_ν), extinction coefficient (β_ν), and the depth of medium or transfer path ($\mathrm{d}s$), and can be expressed as (Liou, 2002, Equation 1.42):

$$\mathrm{d}I_\nu = -I_\nu\beta_\nu\,\mathrm{d}s \tag{2.12}$$

where the subscript ν shows the frequency dependency. The extinction coefficient is equal to the sum of absorption coefficient (κ_ν) and scattering coefficient (σ_ν): $\beta_\nu = \kappa_\nu + \sigma_\nu$. The scattering coefficient integrated over the path-length is referred to as optical depth or opacity:

$$\tau\left(s_2; s_1\right) = \int_{s_1}^{s_2} \beta_\nu \, \mathrm{d}s \tag{2.13}$$

In a non-scattering medium, e.g., clear sky conditions, scattering coefficient is equal to zero, thus $\beta = \kappa$. We assume a non-scattering medium hereafter, unless explicitly stated otherwise. Therefore, in Equation 2.12, β can be replaced with κ as follows:

$$\mathrm{d}I_\nu = -I_\nu \kappa_\nu \, \mathrm{d}s \tag{2.14}$$

Equation 2.14 can be integrated over the path-length which leads to the well-known Lambert-Beer's law:

$$I_\nu = I_\nu(0) \exp\left[-\int_{s_0}^{s_1} \kappa_\nu\left(s\right) \, \mathrm{d}s\right] \tag{2.15}$$

where $I_\nu(0)$ is the incident intensity at s_0, and $\mathrm{d}s$ is the path-length (Chandrasekhar, 2011; Liou, 2002).

In a non-scattering medium, Equation 2.13 can also be expressed in differential form as follows:

$$\mathrm{d}\tau = -\kappa_\nu \, \mathrm{d}s \tag{2.16}$$

If we define transmission (Γ) as the ratio of the outgoing intensity, I_ν, to the incident intensity, $I_\nu(0)$, then:

$$\frac{I_\nu}{I_\nu(0)} = e^{-\tau} \implies \Gamma = e^{-\tau} \tag{2.17}$$

Equation 2.14 only takes absorption into account, however the Earth's atmosphere absorbs and emits at the same time. The RTE which takes into account both absorption and emission terms can be expressed in its differential form as follows (Chandrasekhar, 2011; Liou, 2002):

$$\begin{aligned} \mathrm{d}I_\nu &= -I_\nu \kappa_\nu \, \mathrm{d}s + \kappa_\nu S_\nu \, \mathrm{d}s \\ \frac{\mathrm{d}I_\nu}{\kappa_\nu \, \mathrm{d}s} &= -I_\nu + S_\nu \end{aligned} \tag{2.18}$$

where S_ν is the source function and in a non-scattering medium, in LTE, is equivalent to the Plank function, i.e., $S_\nu = B_\nu$ (Chandrasekhar, 2011, Equation 42).

The *differential equation of radiative transfer* can be derived from Equation 2.18 by replacing $\kappa_\nu \, \mathrm{d}s$ with $-\mathrm{d}\tau$, see Equation 2.16, as follows:

$$\frac{\mathrm{d}I_\nu}{\mathrm{d}\tau_\nu} = I_\nu - B_\nu \tag{2.19}$$

By re-arranging the terms in Equation 2.19, multiplying both sides by $exp(-\tau_\nu)$, then integrating from $s = 0$ to $s = s_1$, we can derive the following equation which is often known as *the integral form of the radiative transfer equation* (Chandrasekhar, 2011; Liou, 2002):

$$I_\nu = I_\nu(0)\, e^{-\tau(s_1;0)} + \int_0^{s_1} \kappa_\nu\,(s)\, B_\nu\,(T\,(s))\, e^{-\tau(s_1;s)}\, \mathrm{d}s \tag{2.20}$$

Plane Parallel Atmosphere

By assuming a plane parallel atmosphere, the path-length (s) can be calculated using vertical coordinate (z) as $z = s\cos\theta \implies \mathrm{d}z = \cos\theta\, \mathrm{d}s$, where θ is the angle between the normal vector and direction of propagation, see Figure 2.2. Now, Equation 2.18 can be expressed in vertical coordinate as follows:

$$\mu \frac{\mathrm{d}I_\nu}{\kappa_\nu \, \mathrm{d}z} = -I_\nu + B_\nu \tag{2.21}$$

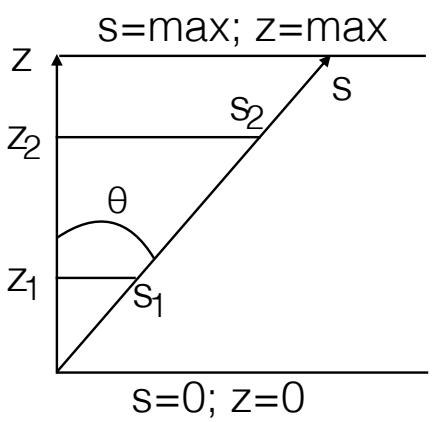

Figure 2.2: *Relation between vertical coordinate (z) and path-length (s).*

where $\mu = \cos(\theta)$. Likewise, optical depth can be defined in vertical coordinate (z direction):

$$\tau(s_2; s_1) = \frac{1}{\mu} \int_{z_1}^{z_2} \kappa_\nu \, \mathrm{d}z = \frac{1}{\mu} \tau(z_2; z_1) \tag{2.22}$$

Now Equation 2.21 can be rewritten as follows:

$$\mu \frac{\mathrm{d}I_\nu}{\mathrm{d}\tau} = I_\nu - B_\nu \tag{2.23}$$

Note that the optical depth is now in vertical coordinate. The integral form of Equation 2.23 can be derived by integrating from surface ($z = 0$) to the satellite receiver where z is equal to the satellite altitude (z_s):

$$I_\nu = I_\nu(0)\, e^{-\tau^*/\mu} + \frac{1}{\mu} \int_0^{z_s} \kappa_\nu(z)\, B_\nu(T\,(z)) e^{-\tau(z_s; z)/\mu} \, \mathrm{d}z \tag{2.24}$$

where τ is zero at the top of atmosphere and maximum at the surface (τ^*), the first and second terms show the surface and atmospheric contributions, respectively. Note that $I_\nu(0)$ includes both emitted and reflected intensities by the surface.

The downwelling intensity that is originated from either the Earth's atmosphere or cosmic cold space (with an approximate temperature of $T_c = 2.7\,\mathrm{K}$), and is reflected by the surface back to the atmosphere can be explicitly included in RTE. In a non-scattering atmosphere, the complete RTE which takes into account surface emission, surface reflectance, atmospheric absorption, and atmospheric emission can be expressed as follows:

$$\begin{aligned} I_v &= \varepsilon B(T_s) \Gamma(z_s; 0) + (1 - \varepsilon) \Gamma(z_s; 0) \\ &\left[B(T_c) \Gamma(z_s; 0) + \frac{1}{\mu} \int_0^{z_s} \kappa(z) B(T(z)) \Gamma(z; 0) \, \mathrm{d}z \right] \\ &+ \frac{1}{\mu} \int_0^{z_s} \kappa(z) B(T(z)) \Gamma(z_s; z) \, \mathrm{d}z \\ \Gamma(z_2; z_1) &= \exp(\frac{-1}{\mu} \int_{z_1}^{z_2} \kappa \, \mathrm{d}z) \end{aligned} \tag{2.25}$$

So far, we have only considered emission and absorption, but scattering also occurs in the presence of particles. The differential form of RTE which includes absorption, emission, and scattering can be expressed as follows:

$$\mu \frac{\mathrm{d}I_\nu}{\mathrm{d}z} = -\beta_\nu I_\nu + \kappa_\nu B(T) + \frac{1}{4\pi}\int_{4\pi} I_\nu(\Omega')P(\Omega,\Omega')\mathrm{d}\Omega' \tag{2.26}$$

where P is the phase function. The first term on the right side of the equation indicates absorption, second term indicates the thermal source, and the last term indicates scattering into the line of sight (Chandrasekhar, 2011; Liou, 2002). There is no analytical solution for Equation 2.26, thus this equation can only be solved using numerical methods which is outside the scope of this thesis.

2.5 Polarization Response

The Stokes parameters are conventionally used to describe the polarization state of propagating radiation and are often combined into a vector known as the Stokes vector (**s**):

$$\mathbf{s} = \begin{pmatrix} s_0 \\ s_1 \\ s_2 \\ s_3 \end{pmatrix} = \begin{pmatrix} I \\ Q \\ U \\ V \end{pmatrix} = \frac{1}{2}\sqrt{\frac{\varepsilon}{\mu}} \begin{pmatrix} \langle E_v E_v^* + E_h E_h^* \rangle \\ \langle E_v E_v^* - E_h E_h^* \rangle \\ \langle E_v E_h^* - E_h E_v^* \rangle \\ \langle E_h E_v^* - E_v E_h^* \rangle \end{pmatrix} \tag{2.27}$$

where E_v and E_h are the components of the electric field with vertical and horizontal polarization, respectively, $*$ indicates the complex conjugate, $< \bullet >$ shows the time average, I is the total (polarized and unpolarized) intensity, Q is the difference between vertical and horizontal components of polarized intensity, U is the difference between the components of linearly polarized intensity oriented at 45° and −45°, and V is the difference between right-hand and left-hand circularly polarized intensities (Berry et al., 1977; Mishchenko et al., 1999). The degree of polarization is calculated as $D_p = \sqrt{Q^2 + U^2 + V^2}/I$.

The measured intensity (I_p), if assuming no losses, is the product of sensor polarization response (**p**) and Stokes vector:

$$I_p = \frac{1}{2}\mathbf{ps} \tag{2.28}$$

where **p** is a four element vector and describes the sensor polarization response. For an instrument with single polarization, the first element is 1 and the sum of the square of the second to fourth elements is equal to 1, i.e., $p_2^2 + p_3^2 + p_4^2 = 1$. For instance, ATMS channel 1 measures the intensity that is vertically polarized, thus $\mathbf{p} = [1 \quad 1 \quad 0 \quad 0]$, while for instance, ATMS Channel 3 measures horizontally polarized intensity, thus for this channel $\mathbf{p} = [1 \quad -1 \quad 0 \quad 0]$.

The polarization changes for microwave cross-track sounders while the reflector rotates along the scan direction, thus they measure a mix of horizontal and vertical components of polarization. In this case, a rotation matrix is utilized

to obtain consistency between the polarization direction and sensor response as follows (Liou, 2002, Equation 6.6.12):

$$\mathbf{L}(\chi) = \begin{pmatrix} 1 & 0 & 0 & 0 \\ 0 & \cos 2\chi & \sin 2\chi & 0 \\ 0 & -\sin 2\chi & \cos 2\chi & 0 \\ 0 & 0 & 0 & 1 \end{pmatrix} \tag{2.29}$$

where χ is the rotation angle. The intensity with a mixed polarization (I_{mx}) can be calculated as follows:

$$I_{mx} = \frac{1}{2}\mathbf{pL}(\chi)\,\mathbf{s} \tag{2.30}$$

2.6 Molecular Absorption

Spectral lines are the result of interaction between photons and molecules or atoms. When an absorbing gas is between a strong source of photons and the detector, photons with a given frequency are absorbed and the intensity of radiation in that specific frequency is decreased, which introduces a so-called absorption line. By contrast, if photons are mainly emitted by the gas then an emission line is created. Since in the atmosphere, a gas absorbs and emits at the same time, the net result of absorption and emission determines whether an absorption or an emission line is created. For more information about molecular absorption, the reader is referred to Siegel (2001, Chapter 11), Goody and Yung (1989, Chapters 3-5), Liou (2002, Chapter 1) and similar references.

The absorption of a given gas is characterized by its absorption coefficient, which itself depends on the number density of molecules (n), and the molecular absorption cross section (α). The absorption coefficient of a medium is summed up for different absorbers (i) as follows:

$$\kappa_\nu = \sum_i n_i \alpha_{\nu i} \tag{2.31}$$

Molecular absorption cross sections depend on several parameters including frequency (ν), line center frequency (ν_0), temperature dependent line strength, $S(T)$, and the normalized line shape, $g(\nu, \nu_0)$, that describes the broadening mechanism (Janssen, 1993, Chapter 2). The monochromatic absorption cross section of a given species at the frequency ν is written as follows:

$$\alpha_\nu = \sum_j S_j(T) g_j(\nu, \nu_{0j}) \tag{2.32}$$

where j indicates the contribution due to a single transition. The center and strength of the lines are given in spectroscopy databases such as the **Hi**gh Resolution **Tran**smission molecular absorption database (HITRAN) (Rothman et al., 2009). The line strength depends on temperature, therefore it is required to be adjusted with temperature:

$$S(T) = S(T_0)\frac{Q(T_0)}{Q(T)}\frac{e^{-E_l/kT}\left(1-e^{-E_u/kT}\right)}{e^{-E_l/kT_0}\left(1-e^{-E_u/kT_0}\right)} \tag{2.33}$$

where $S(T_0)$ is the line strength at a reference temperature (T_0), Q is partition function, E_l in the energy of the lower level of transition, and E_u is the energy of the upper level of transition (Thomas and Stamnes, 2002, Chapter 4). The spectroscopic databases provide $S(T_0)$, the partition function, and the energy for the lower level (E_l). The energy for the upper level (E_u) is calculated as $E_u = E_l + hv$ (Buehler et al., 2005; Rothman et al., 2009).

Each spectral line has its maximum intensity at a given frequency that is called the line center frequency, but it extends over a range of frequencies. Three phenomena contribute to the line broadening: (i) the lifetime of the excited state, (ii) the red and blue shift due to the thermally induced velocity of the gas molecules, and (iii) the collision between the gas molecules. The effects of these phenomena are referred to as natural, Doppler and pressure (collisional) broadening. In atmospheric RTM, natural broadening is negligible and pressure broadening is the most important broadening (Thomas and Stamnes, 2002).

The atoms in a gas have a wide range of velocities that depend on the temperature of the gas. Emitted and absorbed photons, depending on the velocity of the atoms with respect to the absorber, will be either red or blue shifted due to the Doppler effect. The red and blue shifts cause a broadening that is called thermal Doppler broadening and is dominant in the mesosphere for microwave frequencies (Peach, 1981; Thomas and Stamnes, 2002; Thorne et al., 1999). Because of the random nature of the velocity of the molecules in the atmosphere, Doppler broadening can be described by a Gaussian (Doppler) line shape:

$$F_D\left(\nu,\nu_0\right) = \frac{1}{\gamma_D\sqrt{\pi}}\exp\left[-\left(\frac{\nu-\nu_0}{\gamma_D}\right)^2\right] \tag{2.34}$$

where $\gamma_D = \frac{\nu_0}{c}\sqrt{\frac{2kT}{m}}$ is the Doppler width, and m is the mass of the molecule (Liou, 2002; Thomas and Stamnes, 2002).

If an absorbing atom that generates a transition has frequent collision with other atoms, its energy levels will be distorted which causes a line broadening known as collisional or pressure broadening. The collisional broadening is more complicated than Doppler broadening and the calculation of the line shape relies on

approximations. The impact approximation is the most popular approximation for the collisional line-shape and assumes that the duration of collisions is short compared to the time between the collisions. The impact approximation for the collisional broadening results in the Lorentzian line shape (Liou, 2002; Peach, 1981):

$$F_L(\nu, \nu_0) = \frac{\gamma_L}{\pi} \frac{1}{(\nu - \nu_0)^2 + \gamma_L^2} \tag{2.35}$$

where γ_L is the Lorentz line-width. Doppler and collisional broadening occur simultaneously in nature, therefore they cannot be modeled separately. If we assume that these two processes are independent, then the combined process can be modeled by the Voigt line-shape which is the convolution of Doppler and Lorentzian line shape (Liou, 2002; Thomas and Stamnes, 2002):

$$F_V(\nu, \nu_0) = \int F_L(\nu, \nu') F_D(\nu', \nu_0) \, \mathrm{d}\nu' \tag{2.36}$$

No analytical solution exists for the Voigt line-shape, but it can be computationally simplified to other forms as follows (Kuntz and Höpfner, 1999):

$$F_V(\nu, \nu_0) = \frac{1}{\gamma_D \sqrt{\pi}} \frac{y}{\pi} \int_{-\infty}^{+\infty} \frac{\exp(-t^2)}{y^2 + (x - t)^2} \, \mathrm{d}t \tag{2.37}$$

where x is distance from the line center in the unit of Doppler half-width, i.e., $x = (\nu - \nu_0)/\gamma_D$, and y indicates the ratio of Lorentzian to Doppler line-width, i.e., $y = \gamma_L/\gamma_D$. The Voigt line-shape approaches Lorentzian and Doppler line-shapes at some limits (Kuntz and Höpfner, 1999).

The overall effect of absorption by different gases as well as continuum absorption is that the emitted radiance measured by a spaceborne instrument significantly changes with frequency as well as the amount of absorbers. Figure 2.3 shows an example of the opacity in microwave spectrum calculated using the Atmospheric Radiative Transfer Simulator (ARTS) (Eriksson et al., 2011).

2.7 Surface Emissivity

As is shown in Equation 2.6, the amount of radiation emitted by any surface, often known as surface contribution in atmospheric remote sensing, depends on the surface emissivity and temperature. The surface contribution is especially important for window channels where the atmospheric transmission is high and the emitted radiation from the surface can escape the atmosphere and reach the satellite instrument. The surface emissivity in microwave spectrum significantly differs over land and ocean. The ocean surface emissivity is low, around 0.5 to 0.7, while the land surface emissivity is high, around 0.9. Since the in-situ

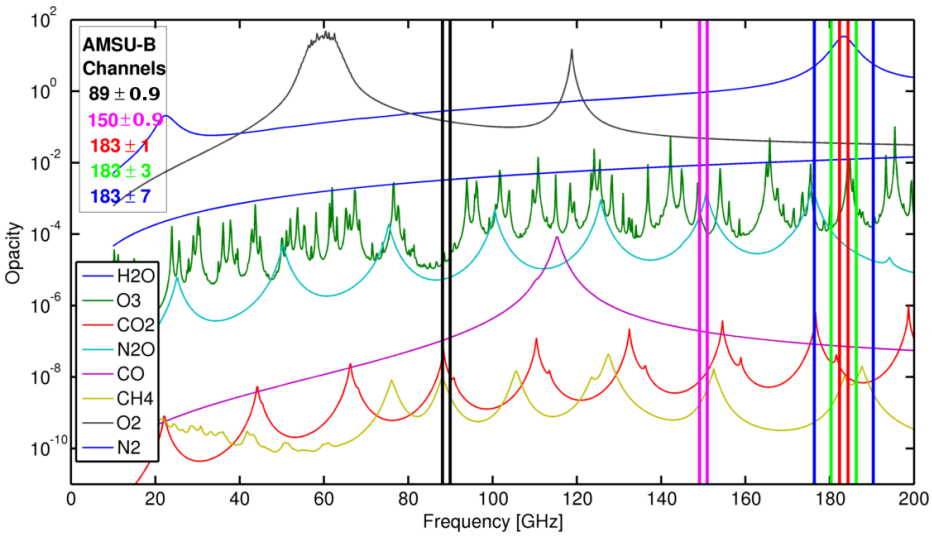

Figure 2.3: *Optical depth at microwave frequencies ranging from* 10 GHz *to* 200 GHz *calculated using ARTS radiative transfer model. Color-bars show the position of AMSU-B channels.*

measurements of surface emissivity are not available, surface emissivity is derived using alternative methods. Surface emissivity in the microwave spectrum is derived differently over land and ocean.

The emissivity over land is derived by inverting the RTE and then using satellite data as input (Jones and Vonder Haar, 1997; Karbou and Prigent, 2005; Matzler, 2005; Prigent et al., 1997). The RTE can be written in brightness temperature unit by taking into account the Rayleigh-Jeans approximation (see Equation 2.4) to replace radiance with temperature in Equation 2.25 :

$$\begin{aligned} T_b &= \varepsilon T_s \Gamma\left(z_s;0\right) + (1-\varepsilon)\Gamma\left(z_s;0\right) T_a\downarrow + T_a\uparrow \\ T_a\uparrow &= \frac{1}{\mu}\int_0^{z_s} \kappa(z) T(z) \Gamma\left(z_s;z\right)\, \mathrm{d}z \\ \Gamma\left(b;a\right) &= \exp\left[-\frac{1}{\mu}\tau\left(b;a\right)\right] = \exp\left[-\frac{1}{\mu}\int_a^b \kappa_\nu\, \mathrm{d}z\right] \end{aligned} \tag{2.38}$$

where $T_a\downarrow$ and $T_a\uparrow$ are downwelling and upwelling atmospheric intensities at the surface and top of atmosphere, respectively, θ is the earth incidence angle, and T_b is the intensity measured by the instrument (Karbou and Prigent, 2005; Matzler, 2005). Note that in Equation 2.38, the contribution from the cold space is ignored because it is not important for emissivity calculations. The emissivity equation is derived by re-arranging the terms in Equation 2.38 as follows:

$$\varepsilon = \frac{T_b - [T_a\uparrow + T_a\downarrow \Gamma(z_s;0)]}{(T_s - T_a\downarrow)\,\Gamma(z_s;0)} \tag{2.39}$$

The land surface can be either considered specular or Lambertian. In the case of specular reflection, that is only valid for very smooth surfaces, radiation reflected by the surface is only originated from the specular angle (Karbou and Prigent, 2005). In this case, $T_a\downarrow$ is calculated as follows:

$$T_a\downarrow = \frac{1}{\mu}\int_0^{z_s} \kappa(z)T(z)\Gamma(z;0)\,\mathrm{d}z \tag{2.40}$$

The reflection by very rough surfaces is determined using Lambertian reflection, where $T_a\downarrow$ is isotropically reflected by the surface. Unlike specular reflection, Lambertian reflection does not introduce polarization and can be calculated as follows (Karbou and Prigent, 2005):

$$T_a\downarrow = \int_0^{\pi/2} 2\sin\theta\cos\theta \left[\frac{1}{\mu}\int_0^{z_s} \kappa(z)\,T(z)\,\Gamma(z;0)\,\mathrm{d}z\right]\mathrm{d}\theta \tag{2.41}$$

The emissivity over sea or ocean can be calculated using more theoretical concepts by employing the Fresnel equations (Meissner and Wentz, 2004, 2012). As shown in Meissner and Wentz (2004, 2012), the surface emissivity over ocean has three components as follows:

$$\varepsilon = \varepsilon_0 + \Delta\varepsilon_w + \Delta\varepsilon_\phi \tag{2.42}$$

where ε_0 is the emissivity of the specular ocean surface, $\Delta\varepsilon_w$ is the isotropic wind induced emissivity which depends on the wind speed, and $\Delta\varepsilon_\phi$ is the four Stokes parameters of the wind direction signal. The first term, ε_0, is the largest component and can be calculated using Fresnel's equation:

$$\begin{aligned} \varepsilon_{0,p} &= 1 - |r_p|^2\,, p = v, h \\ r_v &= \frac{\epsilon\cos\theta - \sqrt{\epsilon - \sin^2\theta}}{\epsilon\cos\theta + \sqrt{\epsilon - \sin^2\theta}} \\ r_h &= \frac{\cos\theta - \sqrt{\epsilon - \sin^2\theta}}{\cos\theta + \sqrt{\epsilon - \sin^2\theta}} \end{aligned} \tag{2.43}$$

where ϵ is the complex dielectric constant. In the microwave spectrum, the complex dielectric constant of water can be calculated using, for instance, the Debye expression presented in Klein and Swift (1977).

Most microwave cross-track sounders operate at a single polarization, but since they employ a rotating antenna the exact polarization response depends on the earth incidence angle. Due to the polarization effect of the water, it is required to take both V and H polarization into account for the radiative transfer calculations.

In cases that all Stokes parameters must be considered, the H and V components of the polarized radiation can be separately calculated using the corresponding emissivity values given by Equation 2.43. In this case, the intensity with mixed polarization can be calculated using Equation 2.30. However, for scalar RTE where only the first Stokes parameter is considered, the emissivity value with mixed polarization at the surface should be calculated using Equation 2.30 in order to perform the RT calculations. The emissivity with mixed polarization can also be calculated using a simplified version of Equation 2.30, by assuming that the U component of Stokes vector is zero. In this case, the emissivity with mixed polarization only depends on the earth incidence angle (θ) and scan angle (ϕ) (Karbou et al., 2006):

$$\varepsilon\left(\nu,\theta,\phi\right)=\varepsilon_{v}\left(\nu,\theta\right)\cos^{2}\phi+\varepsilon_{h}\left(\nu,\theta\right)\sin^{2}\phi \tag{2.44}$$

2.8 Jacobians and Weighting Functions

As discussed before, the absorption coefficient depends on several parameters such as the amount of the absorber, temperature, pressure, and frequency of the photons. These parameters (excluding frequency) change with altitude, thus the absorption coefficient also changes with altitude. The radiance emitted from each layer depends on the absorption coefficient and temperature of that specific layer. However, the emitted radiance needs to pass through all the layers above it to reach the satellite sensors. The emitted radiance will likely be affected by those layers. In some cases, the emitted radiance may completely be absorbed by the layers above it and not reach the sensor at all. Therefore, a microwave instrument (channel) mounted on a satellite may only observe a specific layer of the atmosphere that can vary from the Earth's surface to stratosphere depending on the frequency.

Sensitivity of the measured radiance to the amount of absorbers in different layers of the atmosphere can be described using Jacobians. Jacobians are the partial derivative of the measured radiance with respect to a specific absorber and show the sensitivity of the measured radiance to the partial change in the amount of absorber at different levels. The unit of Jacobians is defined based on the absorber quantity that it perturbed. Two different methods can be used to derive the Jacobians. The first method is called the perturbation method and derives the Jacobians by altering the amount of absorber at different levels then evaluating the impact on measured radiances:

$$K_j = \frac{Tb\,(x_j + \Delta x_j) - Tb\,(x_j - \Delta x_j)}{2\Delta x_j} \tag{2.45}$$

where x is the atmospheric state variable (absorber), e.g., water vapor, at the j-th level, and Δx is defined as a small percentage of x. This relation describes change in brightness temperature (in Kelvin) due to a small change in the concentration (Garand et al., 2001). Jacobians can have either positive or negative sign, where negative sign means that increase in the concentration of the absorber, e.g., water vapor, lowers the observed radiance and vice verse. Jacobians calculated using the perturbation method are approximative. Furthermore, the perturbation method is computationally expensive as the radiative transfer calculations need to be repeated for each perturbation and each layer separately. Therefore, it is preferred to derive Jacobians using analytical solution. For more information about the analytical solution for the Jacobians, the reader is referred to Rodgers (2000) and Buehler et al. (2005).

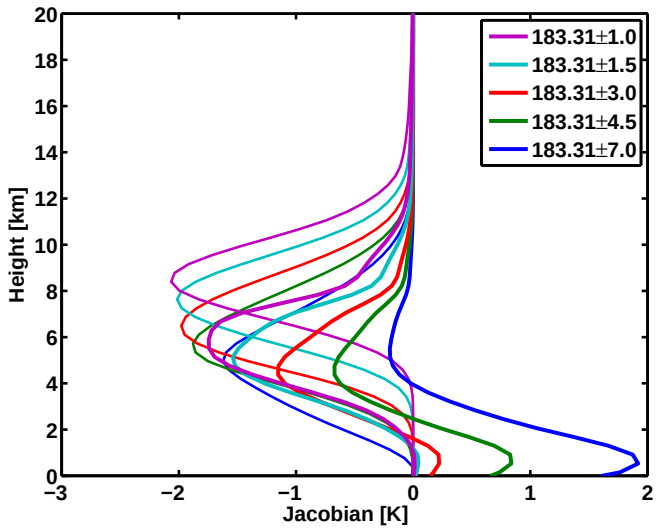

Figure 2.4: *Humidity Jacobians for ATMS water vapor channels. Legend shows the frequency of the channels in GHz. Thin lines are for a tropical profile and thick lines are for a sub-polar winter profile.*

Weighting functions indicate the contribution of the radiance emitted from each layer of the atmosphere to the radiance measured by the satellite instrument. Unlike Jacobians that indicate the sensitivity of the measured radiance to the perturbation of a specific absorber, weighting functions show the net impact of all the absorbers on the measured radiance. Jacobians can be either positive or negative depending on the impact of perturbation on the measured radiance, but weighting functions can only be positive or zero (when the radiance emitted

from a layer is absorbed and does not contribute to the measured radiance). The weighting functions can be mathematically derived using atmospheric transmittance as follows.

$$W_k = \frac{\mathrm{d}\Gamma}{dz} \tag{2.46}$$

where Γ is atmospheric transmittance from the layer k to top of atmosphere (Liou, 2002, Chapter 7). Sample weighting functions for ATMS and SAPHIR water vapor channels are shown in Figure 2.5.

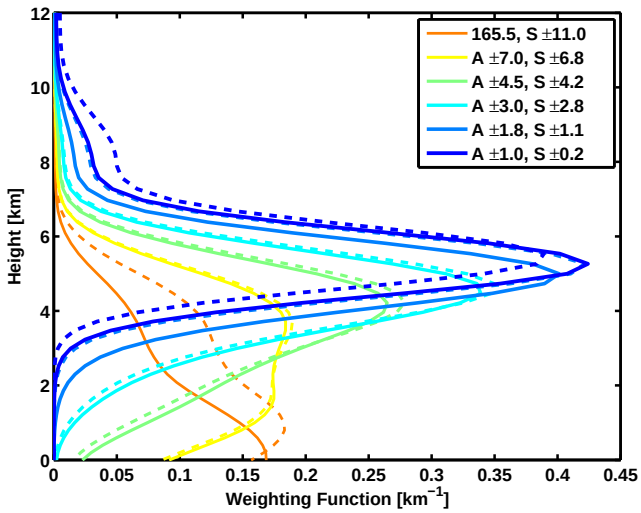

Figure 2.5: *Weighting functions for ATMS and SAPHIR water vapor channels. The legend shows the frequency of the channels with respect to the water vapor absorption line at* 183 GHz*, A stands for ATMS channels (solid lines) and S indicates SAPHIR channels (dashed lines).*

3

Satellite Microwave Instruments

In atmospheric remote sensing, microwave radiometers are widely used to measure radiation emitted or scattered from the Earth's system, including surface, atmosphere, hydrometers, and clouds. This chapter introduces heterodyne microwave receivers, the spaceborne microwave instruments used in this study, as well as the calibration and geolocation of microwave satellite data. It should be noted that satellite data are subject to errors and uncertainties, however these errors are not discussed in this chapter, since several of the publications have focused on the characterization and correction of these errors.

3.1 Microwave Radiometry

Microwave radiometers are used to detect electromagnetic signals in the microwave spectrum with frequencies ranging from a few 100 MHz to several 100 GHz. This corresponds to wavelengths ranging from as long as a meter to a few millimeter. This frequency range is also known as radio-frequency and hereafter we refer to signals with a frequency within this range as RF signals or for simplicity RF.

3.1.1 Microwave Heterodyne Receivers

All microwave instruments used in this research employ a so-called heterodyne receiver. These receivers convert the received RF signal to a signal with a lower frequency, known as intermediate frequency (IF). Figure 3.1 shows a simplified version of a heterodyne receiver which is also known as a total power radiometer. The antenna focuses the incoming signal into a transition line known as waveguide. In this simple example, the received RF signal is first amplified, then

mixed with a local signal (LO) with a known constant frequency generated by a local oscillator. This results in a signal whose frequency (ν_{IF}) is the difference between the frequencies of the received and local signal, $\nu_{IF} = |\nu_{RF} - \nu_{LO}|$. It is very difficult to deal with high frequency microwave signals, but the converted signal with a considerably lower frequency can be processed more conveniently.

The mixer is a non-linear element that generates signals with both sum and difference frequencies, i.e., $\nu_{RF} \pm \nu_{LO}$. The output of the mixer also includes both RF and LO signals as well as some additional signals with higher order inter-modulation frequencies. After amplification, the output of the mixer is filtered to remove the undesired signals such as RF, LO, and higher order signals. The receiver is called low-side injection if the LO frequency is lower than the frequency of the received signal, and high-side injection if the LO frequency is higher than the RF frequency. If the filter only allows a monochromatic signal (a very narrow-band signal) to pass then the corresponding RF signal would also be a monochromatic signal, see Figure 3.2. However, if the filter allows a continuum frequencies ranging from ν_1 to ν_2 to pass then the resulting RF signal would also be a broadband signal, see Figure 3.2.

One of the side effects of the heterodyne receivers is that two different RF signals can generate the same IF signal. For instance, first lets assume a heterodyne receiver with a LO signal with a frequency of 183 GHz and an IF filter that only allows signals with a frequency of 3 GHz to pass. Now, we pass a RF signal with a frequency of 180 GHz through the mixer which produces two signals with frequencies of 180-183=3GHz and 180+183=363 GHz. The filter only allows signals with a frequency of 3 GHz to pass, thus the signal which has a frequency of 363 GHz is removed from the power. Now lets assume a RF signal with a frequency of 186 GHz which generates two signals with frequencies of 3 GHz and 369 GHz. Again, the signal with a frequency of 369 GHz is rejected and the 3 GHz signal passes through the filter. This means that the output of the filter is the summation of intensities from two frequencies that are mirrored with respect to the LO frequency. Although it is possible to remove the unwanted image signal, microwave sounders often retain both the main and the image frequencies, so that the resulting channels are double pass-band as shown in Figure 3.2.

After amplification and filtering, the signal is measured using a square-law detector that converts the incoming current to voltage. The output voltage of square-law detector is proportional to the square of the input current and since $Power = Voltage^2/Current$, thus the output voltage of a square-law detector is proportional to the input power. A DC amplifier is used to intensify the power of the signal. At the end in order to reduce the noise, the incoming signal is integrated over time and finally the signal is digitized and recorded as counts.

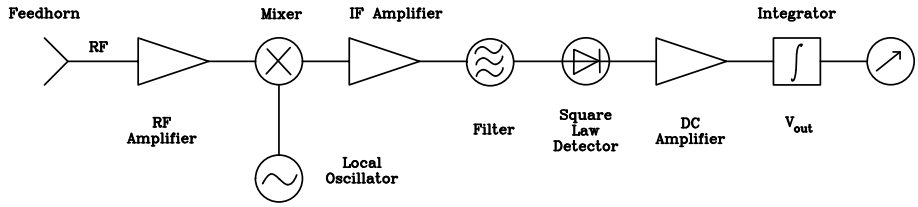

Figure 3.1: *A typical total-power heterodyne receiver where the received signal is mixed with a local signal.*

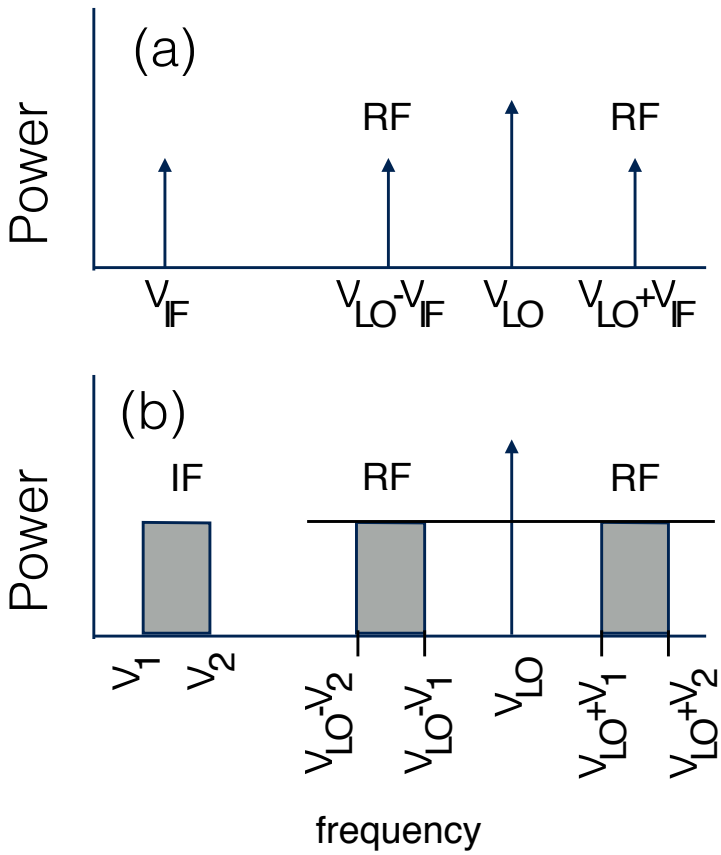

Figure 3.2: *Effect of monochromatic and broadband filters on the frequency translation in heterodyne receivers (adapted from Janssen (1993)).*

3.1.2 Sensor Response Function

Microwave instruments (channels) with a pass-band IF filter operate at a narrow range of frequencies known as the sensor response function. Measured radiances are the convolution of the sensor response function and spectral intensity:

$$\bar{I} = \frac{\int_{\nu_1}^{\nu_2} R_\nu I_\nu \, \mathrm{d}\nu}{\int_{\nu_1}^{\nu_2} R_\nu \, \mathrm{d}\nu} \tag{3.1}$$

where $\bar{I}$ is the instrument measurement, and R_ν is the sensor response function (Wang et al., 2012a).

3.1.3 Antenna Pattern

The antenna pattern, also known as beam pattern, shows the directional (angular) dependence of the intensity of the radiation transmitted by an antenna. An antenna is considered isotropic if it radiates equally in all directions but practically it is not possible to build such an antenna. All the microwave instruments used in this research are passive instruments meaning that antenna is solely used for receiving radiance. According to reciprocity law, fundamental properties of an antenna are identical whether used as a receiver or a transmitter. Thus in this section, sometimes antenna is considered to be transmitting signal rather than receiving, because it is easier to describe the antenna properties in transmitting mode than in receiving mode.

If we define the beam pattern, $E(\theta, \phi)$, as a function of azimuth and zenith angles (ϕ and θ, respectively), then the power pattern is calculated as (Sharkov, 2003):

$$\begin{aligned} P(\theta, \phi) &= E(\theta, \phi) \, E^*(\theta, \phi) \\ P_n(\theta, \phi) &= \frac{P(\theta, \phi)}{P_{max}} \end{aligned} \tag{3.2}$$

where $E^*(\theta, \phi)$ is the complex conjugate of $E(\theta, \phi)$, $P(\theta, \phi)$ is power pattern, and $P_n(\theta, \phi)$ is power pattern normalized with respect to the maximum of the power (P_{max}). The power is normally maximum at the center of the beam, thus $P_{max} = P(0, 0)$. Equation 3.2 shows that the power pattern is positive and real everywhere.

The normalized power is often expressed in decibel (dB). Decibel is a logarithmic scale that is used to express the ratio of two powers or intensities (P_1 and P_2) or the ratio of a power to a reference power and is defined as (Radmanesh, 2009, Appendix I):

$$dB = 10\, log_{10} \left(\frac{P_2}{P_1} \right) \tag{3.3}$$

In the case of normalized power, the reference power is its maximum (P_{max}), thus $dB = 10\, log_{10}\, P_n$. The inverse of this relation can be expressed as $P_n = 10^{\frac{dB}{10}}$. According to this definition, the peak of the power ($P_n = 1$) corresponds to 0 dB and half of the peak ($P_n = 0.5$) corresponds to -3 dB.

The beam pattern is approximately the Fourier transform of the aperture. Since, the aperture of antennas utilized in microwave remote sensing is always a circular disk, their beam pattern can be approximated using the Fourier transform of a uniformly illuminated disk (Russer, 2003, Appendix B). This yields a so-called Bessel function which is shown in Figure 3.3. In one dimensional space, the beam pattern is the Fourier transform of a rectangle that produces a sinc function, $\operatorname{sinc} \alpha = \sin \alpha / \alpha$. Figure 3.4 shows the sinc function as a function of the azimuth angle (ϕ). The direction from which the main beam is transmitted or received is known as main lobe and the lobes around it are called side lobes, see Figure 3.4. In Figure 3.3, the main lobe is the cone in the center of the beam pattern and the side-lobes are the rings around the main lobe. The intensity measured by the receiver (I_{ant}) is the convolution of the intensity received by the antenna, $I(\theta, \phi)$, and the power pattern:

$$I_{ant} = \frac{\iint_{\Omega} I\,(\theta, \phi)\, P_n\,(\theta, \phi) \sin\theta \,\mathrm{d}\theta \mathrm{d}\phi}{\iint_{\Omega} P_n\,(\theta, \phi) \sin\theta \,\mathrm{d}\theta \mathrm{d}\phi} \tag{3.4}$$

Due to the presence of side-lobes in power pattern, the measured intensity by a receiver is not just from the main lobe but also from the side lobes. The antenna pattern correction removes the side lobes' contribution from the measured intensity. For more information on the antenna pattern correction, the reader is referred to Hewison and Saunders (1996) and Weng et al. (2013).

3.1.4 Beam Width

As shown in Figure 3.3, the main power of an antenna is received or transmitted through the main lobe. The main-lobe is normally represented using the beamwidth at 3 dB (θ_{3dB}) and is knows as half-power beam-width (HPBW). HPBW is a function of the size of the antenna as well as frequency (wavelength) and can be approximated using the following equation:

$$\theta_{3dB} \approx 1.22 \frac{\lambda}{D} \tag{3.5}$$

where λ is wavelength, D is the diameter of the antenna (aperture), θ_{3dB} is in radians, and the antenna directional pattern broadens as D/λ decreases. The

resolution of an antenna can be defined as half of the beamwidth between first nulls (FNBW/2) which is approximately equal to HPBW. The effective HPBW can change if the integration of the incoming signals continues while the antenna or the spacecraft are moving. Field of view (FOV) that is defined based on HPBW is denoted as Instantaneous Field of View (IFOV) and indicates the solid angle that is viewed by the instrument at an instantaneous time. However, if the antenna moves while performing the integration of intensity, then the integrated intensity corresponds to a larger solid angle which is denoted as Effective Field of View (EFOV). The IFOV and EFOV are the same in cross-track direction, if the integration is performed while the antenna is stationary, e.g., like AMSU-A instrument, but different if the integration continues while the antenna is moving, e.g., like AMSU-B instrument.

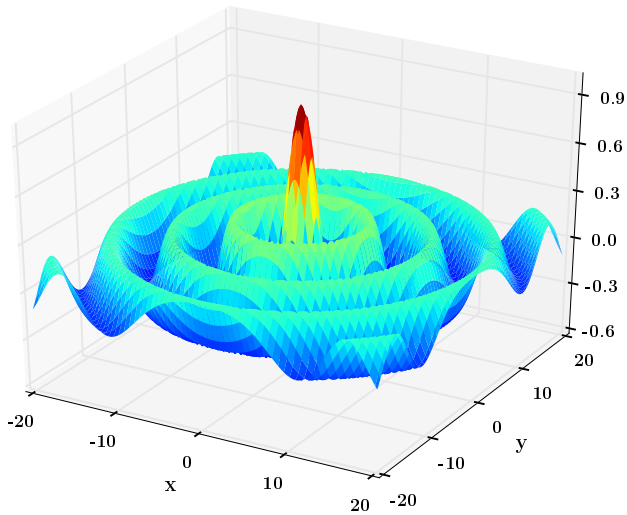

Figure 3.3: *The Bessel function in three dimentional space. The cone in the center of the plot indicates the main lobe and the rings around the main lobe indicate the side lobes.*

3.1.5 Beam Solid Angle

The total antenna (beam) solid angle (Ω_A), also known as beam area, is the solid angle through which all the power would be radiated if the $P(\theta, \phi)$ is maximum over Ω_A and zero elsewhere. The beam solid angle is calculated using normalized power and smaller values of Ω_A shows more directed beams:

$$\Omega_A = \int_{\phi=0}^{\phi=2\pi} \int_{\theta=0}^{\theta=\pi} P_n(\theta, \phi) \sin\theta \, \mathrm{d}\theta \, \mathrm{d}\phi = \iint_{4\pi} P_n(\theta, \phi) \, \mathrm{d}\Omega \tag{3.6}$$

The solid angle (Ω_A) after some transformation can be derived as $\frac{\pi}{4}\theta_{3dB}^2$ which

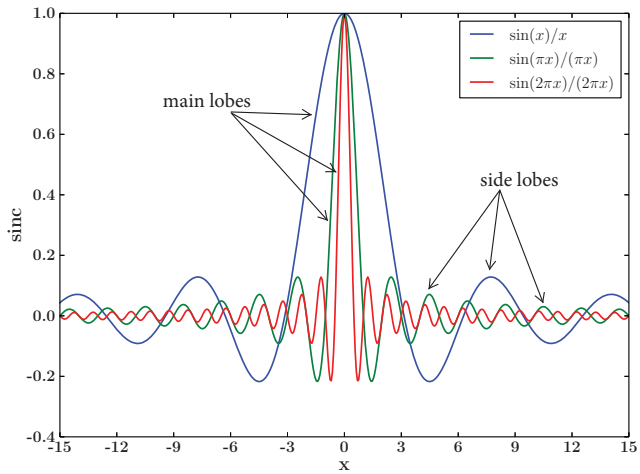

Figure 3.4: *The* sinc *function normalized with respect to x (blue curve), πx (green curve), and $2\pi x$ (red curve).*

gives the solid angle a unit of square degrees that is often used in observational practices (Sharkov, 2003). The main beam solid angle is calculated in a similar way but only over the main beam area:

$$\Omega_B = \iint_{main-lobe} P_n(\theta, \phi)\, \mathrm{d}\Omega \tag{3.7}$$

The total beam solid angle is $\Omega_A = \Omega_B + \Omega_S$, where Ω_S is the side-lobe solid angle.

3.1.6 Directivity

The antenna (maximum) directivity (D_A) is defined as the ratio of the maximum of the power to the average of the power over a sphere in the far field of the antenna and can be calculated as (Baars, 2007; Salvia, 2007; Sharkov, 2003):

$$D_A = \frac{P_{max}}{P_{avg}} = \frac{P_{max}}{\iint P(\theta, \phi)\, \mathrm{d}\Omega / 4\pi} = \frac{4\pi}{\Omega_A} \tag{3.8}$$

Therefore, the directivity is the area of the sphere (4π) over the total beam solid angle (Ω_A). In the other word, Equation 3.8 shows the directional properties of an antenna with respect to a perfect spherical emitter. Antenna directivity is inversely related to the beam solid angle, thus larger solid angles show less directed antennas (Sharkov, 2003). The antenna directivity is equal to one for a spherically symmetric beam, because Ω_A is equal to 4π, and larger values

of directivity corresponds to more directed antennas (Baars, 2007). Antenna directivity can be up to tens or hundred of thousands. The main beam directivity can be defined in the same way as D_A (Sharkov, 2003):

$$D_B = \frac{4\pi}{\Omega_B} \tag{3.9}$$

3.1.7 Noise and Sensitivity

Sensitivity of the detector (receiver) which is often described as noise equivalent temperature difference (NEΔT) can be defined as the minimum temperature difference that can be detected above the noise-level:

$$NE\Delta T = \frac{k_e T_{sys}}{\sqrt{Bt}} \tag{3.10}$$

where T_{sys} is the system temperature, k_e is a constant that depends on the design of the system and antenna, ranging between 1 and 3, B is the bandwidth or passband of the channel, and t is the integration time (Baars, 2007; Woodhouse, 2005). Integration time is the time that is used to integrate the incoming RF signal. Since there is an inverse relation between the integration time and the instrument noise, longer integration time lowers the noise level.

3.2 Satellite Microwave Sounders

Microwave radiometers can be classified into two general categories of sounders and imagers. Imagers are generally used to obtain ground track images and provide information on Earth's surface as well as cloud properties, while microwave sounders are used to acquire the profiles of the atmospheric state variables such as water vapor and temperature (Okamoto, 2000). However, some of sounding channels measure also the intensity emitted or reflected by the Earth's surface. These channels are called window channels and similar to imagers provide information on Earth's surface. In either case, a two dimension image is obtained using the movement of the antenna in one direction and the movement of the platform in the orthogonal direction.

3.2.1 Cross-track and Conical Scanners

The antenna movement can be performed in either cross-track or conical fashion. Both antenna scanning methods are shown in Figure 3.5. All instruments used in this study are cross-track sounders, thus this chapter focuses on this class of microwave instruments. Cross-track sounders include a flat-reflector that rotates perpendicular to the flight direction. Figure 3.6 shows a diagram for the scan sequence of a cross-track scanner. The antenna first views the earth scenes at different scan angles and measures the microwave radiation that falls into the antenna solid angle. The antenna then rotates towards the cosmic background to

scan the cold space calibration point and after that immediately rotates towards and scans the internal blackbody target which is also known as the warm load. As it is explained in Section 3.3, the warm and cold loads are used for calibration. The time required to complete one scan depends on the instrument and varies from 8/3 s for AMSU-B to 8 s for AMSU-A.

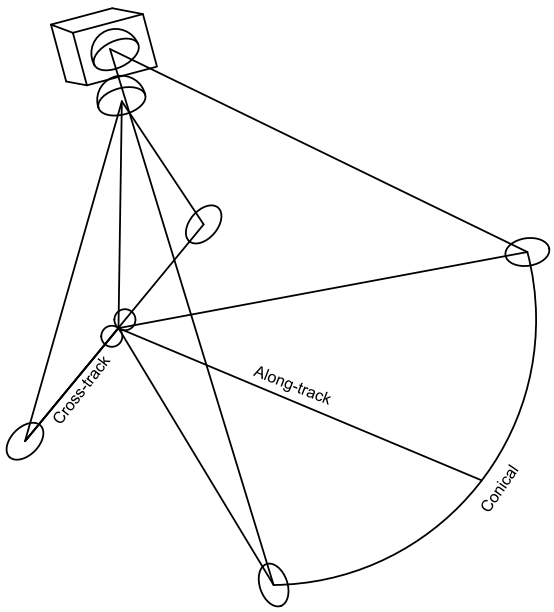

Figure 3.5: *Scan geometry for a conical and a cross-track microwave instrument.*

Some of the main characteristics of a cross-track instrument are shown in Figure 3.7. Note that the scan and earth incidence angles are different, because of the curvature of the earth, and the difference increases towards the edge of the scan.

This research utilized data from five microwave sounders: AMSU-A, AMSU-B, MHS, ATMS, and SAPHIR. Table 3.1 shows the availability of data from different satellites and different instruments. It should be noted that the dates reported in Table 3.1 are with respect to microwave water vapor channels. However, different instruments on the same satellite or even different channels on the same instrument may fail on different dates. Therefore, the dates reported in Table 3.1 may vary up to even a few years depending on the channels of interest. For instance, NOAA-15 AMSU-B Channels 18-20 failed in September 2010 due to an oscillator failure, but channels 16 and 17 are still operating. NOAA 16 was decommissioned on June 9, 2014 due to major spacecraft

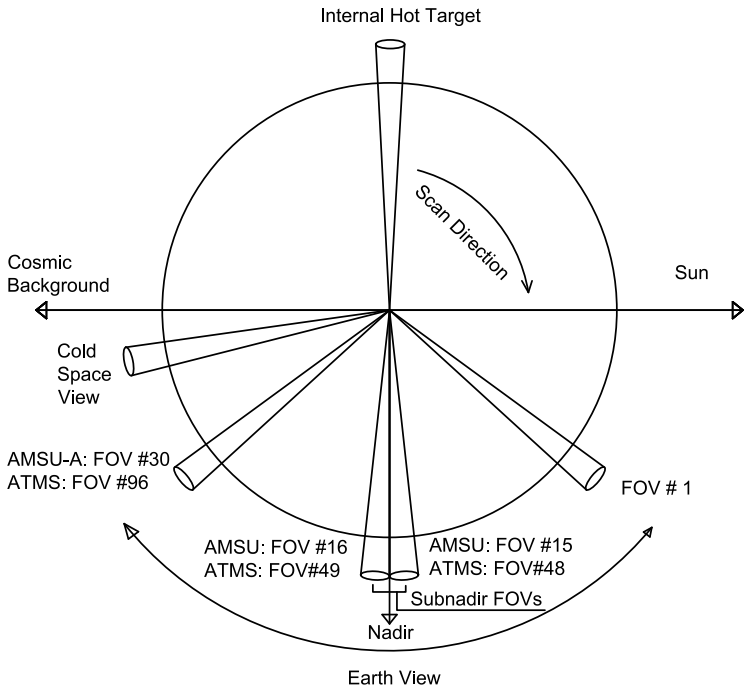

Figure 3.6: *Nominal scan diagram for crosstrack sounders. The satellite flight direction is towards the reader.*

anomaly. NOAA-17 AMSU-B failed in January 2010, but the satellite was decommissioned on April 10, 2013. The current status of these satellites is available at http://www.ospo.noaa.gov/Operations/POES/status.html.

3.2.2 AMSU-A

AMSU-A is a 15 channels total power radiometer operating at frequencies ranging from 23.8 to 89 GHz. The instrument is dedicated to measuring atmospheric temperature profiles (channels 4 to 14), as well as total precipitable water vapor (channels 1 and 2). The window channels of AMSU-A, e.g., Channel 15 at 89 GHz, can also be used for retrieving other geophysical variables such as rain rate, sea ice concentration, and snow cover.

AMSU-A is a stepped-line scanning radiometer meaning that the instrument scans and stops for a very short period of time for integration then moves to the next beam position. Therefore, the IFOV and EFOV are essentially the same for the AMSU-A instrument. AMSU-A has been the main temperature sounder on the NOAA-15 to NOAA-19 as well as the MetOp-A and MetOp-B satellites. One complete scanline of AMSU-A includes 30 beam positions and takes 8 seconds. The swatch width is 2074 km and the field of view translates to about 48 km at nadir and increases toward the edge of the scan.

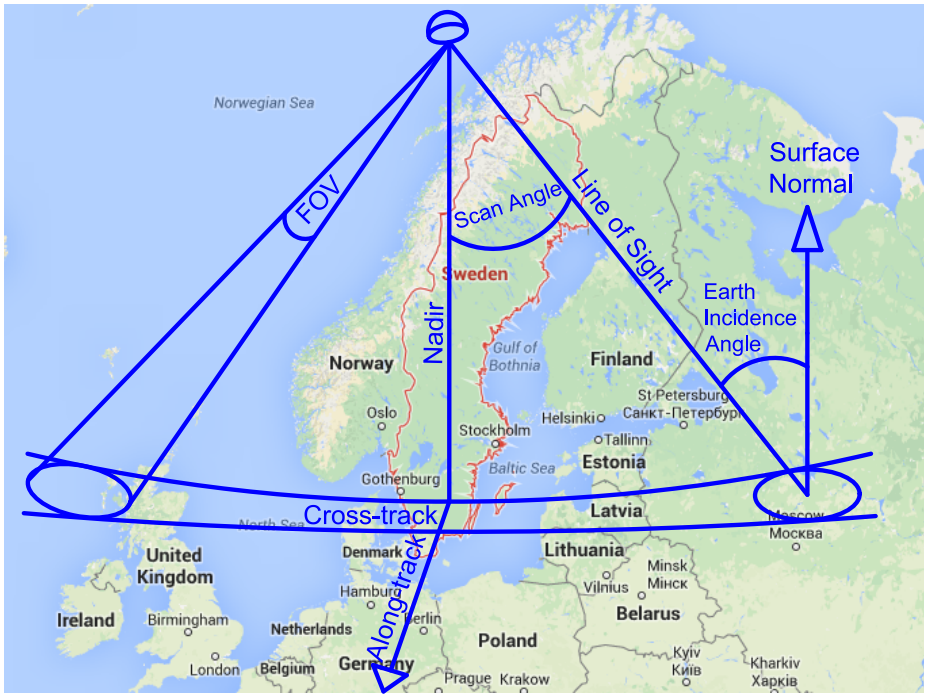

Figure 3.7: *Scan characteristics for a cross-track microwave instrument. Source: background image is from Google Maps.*

The AMSU-A instrument is implemented in two independent modules: AMSU-A1 and AMSU-A2. Each module has a separate spacecraft interface. Channels 1 and 2 that are used for measuring atmospheric moisture are on AMSU-A2. The remaining thirteen channels are on AMSU-A1, which are supported by two antennas. This approach provides a minimum front-end radio frequency loss and also a 3.3° field of view for all the channels (Goodrum et al., 2007). Table 3.2 shows the radiometric characteristics of AMSU-A instrument.

3.2.3 AMSU-B and MHS

AMSU-B and MHS are 5 channel cross track sounders dedicated to measuring atmospheric water vapor at different levels. The characteristics of AMSU-B and MHS are shown in Table 3.3. The MHS sensor is very similar to AMSU-B, but the second channel is moved to 157.0 GHz and the fifth channel has only one passband at 190.311 GHz. Both instruments have 90 beam positions per scanline with an IFOV of 1.1°. However, the step angle, i.e., angular distance between two adjacent beam positions, is $\frac{11}{10}^\circ$ for AMSU-B but $\frac{10}{9}^\circ$ for MHS. The swath width is approximately 2300 km and the earth incidence angle changes from about 0.62° for the innermost scan positions to 58.5° for the outermost scan positions. Both instruments complete one scan line in 8/3 seconds, thus the

Table 3.1: *Data availability from passive microwave sounders used in this study. N15 to N18 indicate NOAA-15 to NOAA-18 satellites. MA, NP, and MT indicate MetOp-A, S-NPP, and Megha-Tropiques satellites, respectively. AMA and AMB stand for AMSU-A and AMSU-B, respectively. The launch date of each satellite in shown in the table.*

Sat.	Sensor	1998	1999	2000	2001	2002	...	2005	2006	...	2009	2010	2011	2012	2013	2014
N15	AMA, AMB	13 May 1998														
N16	AMA, AMB				21 Sep. 2000											
N17	AMA, AMB					24 June 2002										
N18	AMA, MHS							20 May 2005								
MA	AMA, MHS								19 Oct. 2006							
NP	ATMS												17 Oct 2011			
MT	SAPHIR												12 Oct 2011			

Table 3.2: *AMSU-A radiometric and channel characteristics (Goodrum et al., 2007). C. stands for channel number, BDW is bandwidth in MHz, BMW is beamwidth in degrees, Pol. stands for polarization, and Ant. stands for the antenna. Frequency is in GHz, and NEΔT is in Kelvin.*

C.	**Frequency**	**BDW**	**BMW**	**NEΔT**	**Pol.**	**Ant.**
1	23.800	270	3.3	0.30	V	A2
2	31.400	180	3.3	0.30	V	A2
3	50.300	180	3.3	0.40	V	A1-2
4	52.800	400	3.3	0.25	V	A1-2
5	53.596±0.115	170	3.3	0.25	H	A1-2
6	54.400	400	3.3	0.25	H	A1-1
7	54.940	400	3.3	0.25	V	A1-1
8	55.500	330	3.3	0.25	H	A1-2
9	57.290344 [f_0]	330	3.3	0.25	H	A1-1
10	f_0±0.217	78	3.3	0.40	H	A1-1
11	f_0±0.322±0.048	36	3.3	0.40	H	A1-1
12	f_0±0.322±0.022	16	3.3	0.60	H	A1-1
13	f_0±0.322±0.010	8	3.3	0.80	H	A1-1
14	f_0±0.322±0.0045	3	3.3	1.20	H	A1-1
15	89.0	<6000	3.3	0.50	V	A1-1

scanning rate is 3 times faster than that for AMSU-A. There is generally three AMSU-B/MHS scanlines per one AMSU-A scanline. Therefore, the footprint size is approximately one third of that for AMSU-A, about 16 km at nadir but increases towards the edge of the scan. Both AMSU-B and MHS have only a single reflector and feedhorn for all the channels. All AMSU-B channels as well as MHS Channels 1, 2, and 5 have quasi vertical polarization so that at nadir the polarization vector is parallel to the scan plane but rotates with scan angle. MHS Channels 3 and 4 have quasi horizontal polarization so that at nadir the polarization vector is perpendicular to the scan plane but rotates with scan angle.

Table 3.3: *AMSU-B/MHS radiometric and channel characteristics (Goodrum et al., 2007). C. stands for channel number, BDW indicates bandwidth in MHz, and Pol. stands for polarization. Frequency is in GHz, and NEΔT is in Kelvin. All AMSU-B channels have quasi-vertical polarization.*

AMSU-B				MHS			
C.	**Frequency**	**BDW**	**NEΔT**	**Frequency**	**BDW**	**NEΔT**	**Pol.**
1	89.0±0.9	1000	0.35	89.0	2800	0.22	V
2	150.0±0.9	1000	0.84	157.0	2800	0.34	V
3	183.31±1.0	500	1.06	183.31±1.0	500	0.51	H
4	183.31±3.0	1000	0.70	183.31±3.0	1000	0.40	H
5	183.31±7.0	2000	0.60	190.311	2200	0.46	V

3.2.4 ATMS

ATMS is a cross-track microwave sounder with 22 channels operating at microwave frequencies from 23.8 GHz to 190.31 GHz designed to measure atmospheric temperature, water vapor, and many other parameters, such as rain-rate, cloud ice water path, sea ice concentration, and snow cover. ATMS combines all the channels of the preceding instruments (AMSU-A and MHS/AMSU-B) into a single instrument with considerable savings in mass, power, and volume. ATMS has several improvements compared to legacy instruments including wider swath, better resolution, and more channels. ATMS is currently flying on Suomi National Polar-orbiting Partnership (S-NPP) satellite and is planned to fly on the United States next generation polar-orbiting operational environmental satellite system named Joint Polar Satellite System (JPSS). S-NPP was launched in a sun-synchronous orbit in October 2011 with the ascending equatorial crossing time at 13:30 local time. The average altitude of the S-NPP orbit is 824 km with an inclination of 97.1° which yields an orbital period of 101 minutes (Kim et al., 2014). A diagram of S-NPP satellite that shows the location of different instruments on the spacecraft, including ATMS, is shown in Figure 3.8.

ATMS consists of two parabolic reflectors, one serving Channels 1-15 and the other one Channels 16-22. As shown in Figure 3.9, each antenna is served by a flat reflector tilted 45° rotating in cross-track direction and reflects the radiation coming from a solid angle perpendicular to the scan axis into a direction parallel to the scan axis (Baker, 2011). A simplified version of ATMS block diagram is shown in Figure 3.10. The flat rotating reflectors are used to switch between earth views, clod space view, and warm load. The characteristics of ATMS instrument including frequency, band width, beam-width, and polarization are reported in Table 3.4. For more information on the ATMS instrument the reader is referred to Baker (2011) and Kim et al. (2014).

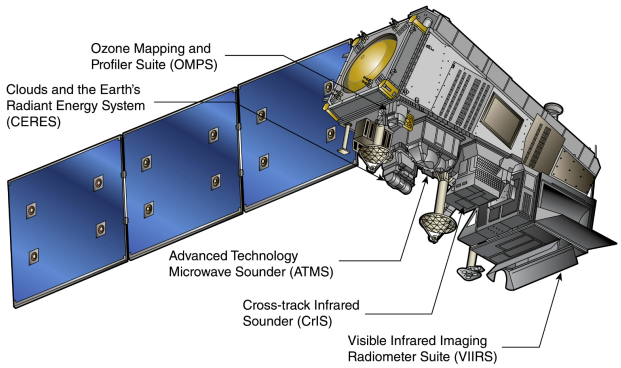

Figure 3.8: *The Soumi NPP Diagram (Baker, 2011).*

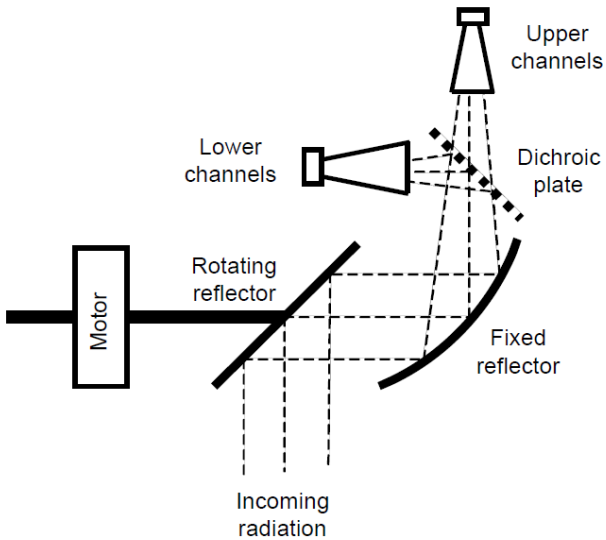

Figure 3.9: *Schematic of ATMS antenna and scanning system (Baker, 2011).*

3.2.5 SAPHIR

SAPHIR is a 6 channel cross-track microwave sounder flying on Megha-Tropiques (M-T) satellite. The M-T altitude is 865 km and the satellite orbit inclination is 19.98°. This means that unlike polar orbiting satellites which cross the equator almost in north-south direction and have global coverage, the M-T satellite crosses the equator with an inclination of 19.98°, and only covers the tropical band between 30 S and 30 N. There was primarily two microwave instruments onboard M-T: Microwave Analysis and Detection of Rain and Atmospheric Systems (MADRAS), and SAPHIR. The MADRAS instrument, whose primary purpose

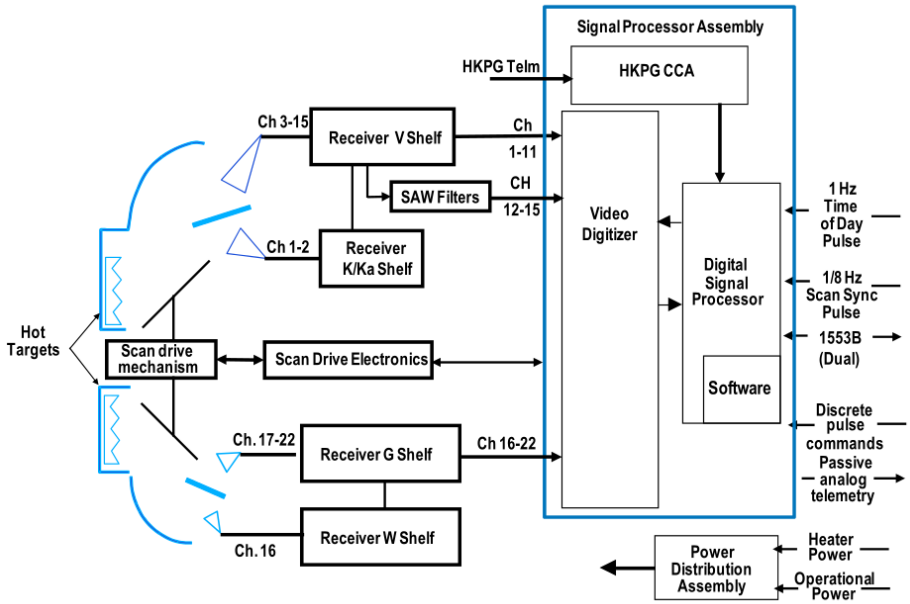

Figure 3.10: *The ATMS block diagram (Kim et al., 2014, used with permission).*

was to measure atmospheric temperature, surface properties, and precipitation, experienced several malfunctions and stopped operating. The channel characteristics of SAPHIR instrument are shown in Table 3.5. All SAPHIR channels have quasi horizontal polarization so that at nadir the polarization vector is perpendicular to the scan plane but rotates with the scan angle. The SAPHIR swath width is 1700 km, and the footprint is 10 km at nadir for all the channels.

3.3 Calibration of Microwave Instruments

All the microwave sounders used in this study have a similar sequence for calibration which is based on scanning a number of earth FOV's, then a cold space view, and immediately after that scanning the warm (hot) load (target) with a brightness temperature similar to the instrument internal ambient temperature, see Figure 3.6. The cold space view and warm load are used to calculate the radiometric transfer function. As shown in Figure 3.11, by assuming a linear transfer function, the antenna radiance can be calculated as follows:

$$\frac{I_E - I_H}{C_E - C_H} = \frac{I_H - I_S}{C_H - C_S} \implies I_E = \frac{C_E - C_H}{C_H - C_S}(I_H - I_S) + I_H \tag{3.11}$$

where I_E, I_S, and I_H indicate the Earth scene, cold space and warm load radiances, and C_E, C_S, and C_H indicate measured counts for Earth scene, cold

Table 3.4: *ATMS radiometric and channel characteristics (Baker, 2011). BDW is bandwidth in MHz, BMW is beamwidth in degrees, Pol. is polarization, Ant. indicates the antenna. Frequency is in GHz, and NEΔT is in Kelvin*

C.	Frequency	BDW	NEΔT	BMW	Pol.	Ant
1	23.80	270	0.5	5.2	V	A
2	31.40	180	0.6	5.2	V	A
3	50.30	180	0.7	2.2	H	A
4	51.760	400	0.5	2.2	H	A
5	52.80	400	0.5	2.2	H	A
6	53.596±0.115	170	0.5	2.2	H	A
7	54.40	400	0.5	2.2	H	A
8	54.94	400	0.5	2.2	H	A
9	55.50	330	0.5	2.2	H	A
10	57.290344 [f0]	330	0.75	2.2	H	A
11	f0±0.217	78	1.0	2.2	H	A
12	f0±0.322±0.048	36	1.0	2.2	H	A
13	f0±0.322±0.022	16	1.5	2.2	H	A
14	f0±0.322±0.010	8	2.2	2.2	H	A
15	f0±0.322±0.0045	3	3.6	2.2	H	A
16	88.20	2000	0.3	2.2	V	B
17	165.50	3000	0.6	1.1	H	B
18	183.31±7.0	2000	0.8	1.1	H	B
19	183.31±4.5	2000	0.8	1.1	H	B
20	183.31±3.0	1000	0.8	1.1	H	B
21	183.31±1.8	1000	0.8	1.1	H	B
22	183.31±1.0	500	0.9	1.1	H	B

Table 3.5: *SAPHIR radiometric and channel characteristics (Team, 2013). C. stands for channel, BDW is bandwidth in MHz, Frequency is in GHz, and NEΔT is in Kelvin*

C.	Frequency	BDW	NEΔT
S1	183.31±0.20	200	2.35
S2	183.31±1.10	350	1.45
S3	183.31±2.80	500	1.36
S4	183.31±4.20	700	1.38
S5	183.31±6.80	1200	1.03
S6	183.31±11.0	2000	1.10

space and warm load. The unit of I_x is either $\mathrm{mW\,m^{-2}\,sr^{-1}\,Hz^{-1}}$ or a similar unit in terms of frequency or wavenumber. There is normally more than one measurement for both cold space and warm load, so the values are averaged for both radiances and counts. The ratio of counts to radiance is defined as the gain of the instrument:

$$G = \frac{C_H - C_S}{I_H - I_S}, \qquad \frac{count}{mW.m^{-2}.sr^{-1}.Hz^{-1}} \tag{3.12}$$

Equation 3.11 assumes that calibration is perfectly linear, however due to imperfect square-law detector, see Figure 3.1, some non-linearity may be involved in the calibration. Thus, a nonlinearity term (Q) is added to Equation 3.11 as follows (Janssen, 1993; Mo, 1996):

$$\begin{aligned} I_E &= \frac{C_E - C_H}{C_H - C_S}\left(I_H - I_S\right) + I_H + Q \\ Q &= \mu\left(I_H - I_S\right)^2 \frac{\left(C_E - C_H\right)\left(C_E - C_S\right)}{\left(C_H - C_S\right)^2} \end{aligned} \tag{3.13}$$

where μ is determined using pre-launch data for three low, nominal, and high temperatures and is interpolated for other temperatures.

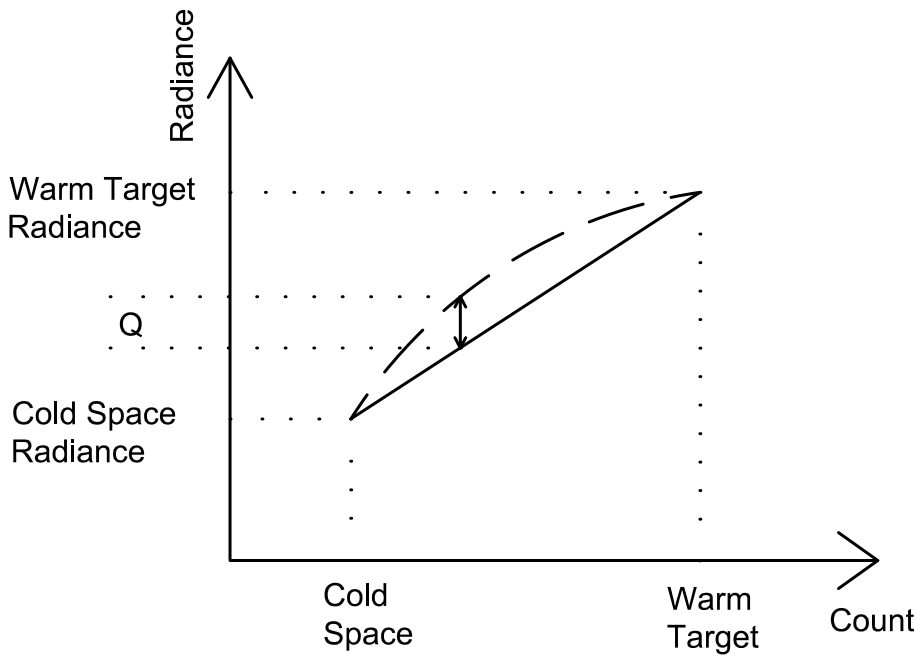

Figure 3.11: *Radiometric transfer function for microwave radiometers with two point calibration system. Solid and dashed lines show a linear and a non-linear transfer functions, respectively, and Q is the nonlinearity term.*

It is preferred to perform the calibration in radiance space then convert the calibrated radiances to brightness temperature using Equation 2.7. However,

according to the Rayleigh–Jeans approximation, see Equation 2.4, the relation between temperature and radiance is linear, thus in Equation 3.11, radiance (I_x) can be replaced with brightness temperature (Tb) as follows:

$$Tb_E = \frac{C_E - C_H}{C_H - C_S}(Tb_H - Tb_S) + Tb_H + Q \tag{3.14}$$

As mentioned before, the Rayleigh–Jeans approximation is not accurate for very low temperatures. The calibration of AMSU-A, AMSU-B, and MHS is performed in radiance space, but the ATMS calibration is currently in brightness temperature space.

3.4 Geolocation of Satellite Data

Geolocation of satellite data refers to determining the earth location of the measured radiances. Geolocation consist of two steps, (i) finding the satellite position in the orbit using either a GPS onboard the satellite or ephemeris data and a propagation model, and then (ii) projecting the satellite position to the earth surface and calculating the earth location of the data. In addition to the geographical coordinates, earth incidence angle is another important quantity that is calculated during geolocation.

Geolocation can be performed using either a geocentric or a geodetic coordinate system. In the geocentric system, the subsatellite point is defined as the intersection of the vector that points from the satellite position to the Earth's center, but in the geodetic system, the subsatellite point is defined as the intersection of the vector that is originated from the satellite position and is normal to the Earth's surface. Moreover, the geocentric latitude is defined as the angle between the equatorial plane and the vector that points from the spot location to the earth's center, but the geodetic latitude is defined as the angle between the normal vector to the Earth's surface at the spot location and the equatorial plane. This section uses a geocentric coordinate system for geolocation, because a geodetic system requires sophisticated calculations that are outside the scope of this section. However, the actual geolocation was performed using a geodetic system throughout the research.

The first step of geolocation is to calculate the satellite state vectors using two line ephemeris (TLE) data and a propagation model. The satellite state vectors are first defined in an Earth-Centered Inertial coordinate system (ECI). In this system, see Figure 3.12, the Z_{ECI} axis points along the spin axis of the Earth. The X_{ECI} axis points from the Earth's center to the vernal equinox, at the intersection of the Earth's equatorial plane and the ecliptic plane of the Earth's orbit around the Sun. The Y_{ECI} axis is on the Earth's equatorial plane perpendicular to X_{ECI} axis. For this discussion, the Earth's spin axis is considered as "true-of-date" and we ignore the detailed effect on the inertial coordinate definition of the Earth's spin axis precession and nutation over time. The Earth-Centered,

Earth-Fixed (ECEF) is similar to ECI but the x-y plane is rotated so that the x-axis points to the Greenwich meridian. ECEF rotates with the Earth, therefore the coordinates of a point fixed on the Earth does not change with time. The relation between ECI and ECEF coordinate systems are shown in Figure 3.12. The following equations are used to convert from ECI to ECEF coordinate system:

$$\begin{aligned} X_{ECEF} &= X_{ECI}\ \cos(G) + Y_{ECI}\ \sin(G) \\ Y_{ECEF} &= Y_{ECI}\ \cos(G) - X_{ECI}\ \sin(G) \\ Z_{ECEF} &= Z_{ECI} \end{aligned} \tag{3.15}$$

where G is the Greenwich Sidereal Hour angle, the angle between Greenwich meridian and vernal equinox, which is a function of time. The ECEF is used to project the satellite position to the Earth's surface and geolocate the satellite data. In a geocentric coordinate, latitude (ϕ) and longitude (λ) of the subsatellite point, see Figure 3.12, are defined as follows:

$$\begin{aligned} \tan\phi &= \frac{Z}{\sqrt{X^2 + Y^2}} \\ \tan\lambda &= \frac{Y}{X} \end{aligned} \tag{3.16}$$

The earth incidence angle, also known as local zenith angle, and scan angles are very important for radiative transfer calculations as they directly affect the optical path length and also the computations for the polarized components of the intensity received by the sensor. Scan angle is the angle between the nadir pointing vector, i.e. the vector that points to the subsatellite point, and the local pointing vector, see Figure 3.12. The earth incidence angle is the angle between the satellite antenna boresight direction and the normal to the Earth's surface at the spot location, see Figure 3.7, and can be calculated as follows:

$$\cos(\theta) = \frac{-R \cdot \tilde{n}}{\|n\|\ \|R\|} \tag{3.17}$$

The surface normal can be calculated as the gradient of the Earth's ellipsoid:

$$\tilde{n} = < \frac{x}{a^2}, \frac{y}{a^2}, \frac{z}{b^2} > \tag{3.18}$$

where x, y, and z are ECEF coordinate system, and a and b are, respectively, the semi-major (equatorial) and semi-minor (polar) axes of the Earth's ellipse. NOAA uses World Geodetic Survey 1972 (WGS-72), therefore $a = 6378.135\,\text{km}$ and $b = 6356.750\,52\,\text{km}$.

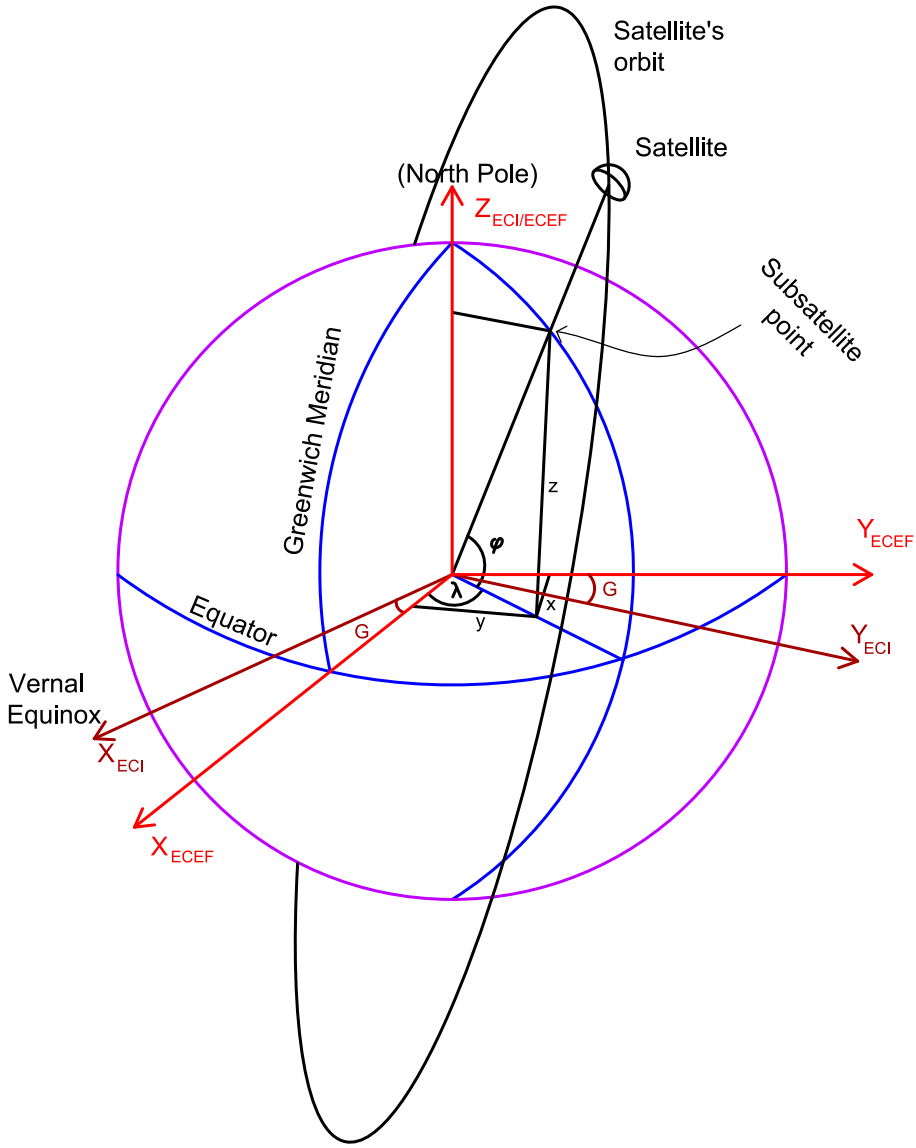

Figure 3.12: *Satellite position and its geometry in different coordinate systems.*

4

Radiosonde Measurements

Radiosonde data are the only source of direct measurement of tropospheric humidity. Although, the primary purpose of radiosonde observations is for weather forecasting and initialization of numerical weather prediction models, these data are extensively used for other applications, such as assimilation into climate reanalysis, validation of satellite observations, long-term climate assessments, and as a-priori to retrieve geophysical variables.

A radiosonde is a small instrument package consisting of several sensors to measure the vertical profile of atmospheric state variables such as water vapor, temperature, wind, and ozone. The package is attached below a weather balloon, made of either rubber or latex and filled with either helium or hydrogen. Figure 4.1 shows a standard radiosonde setup, including balloon, parachute, and the sensor package, that is used at many operational upper air networks. The measurements are transmitted through radio-signal to the ground station (NOAA, 2014). The maximum altitude that a balloon can reach depends on the size and the thickness of the balloon. Some weather balloons may reach up to 30 km, but many of the balloons that are used for operational purposes do not even reach upper troposphere. For instance, at the U.S. upper air network, radiosonde measurements are considered to be minimally acceptable if the balloon reaches 400 hPa. A second radiosonde is only released, if the balloon bursts before reaching 400 hPa pressure level or if the temperature or pressure data are missing for more than 6 minutes (NOAA, 2014).

4.1 Radiosonde Humidity Sensors

Radiosondes can be classified into four general groups with respect to the radiosonde humidity sensor: gold-beater's skin, carbon hygristor, polymer sensor, and frost-point hygrometers. Table 4.1 shows the type of the radiosonde sensors,

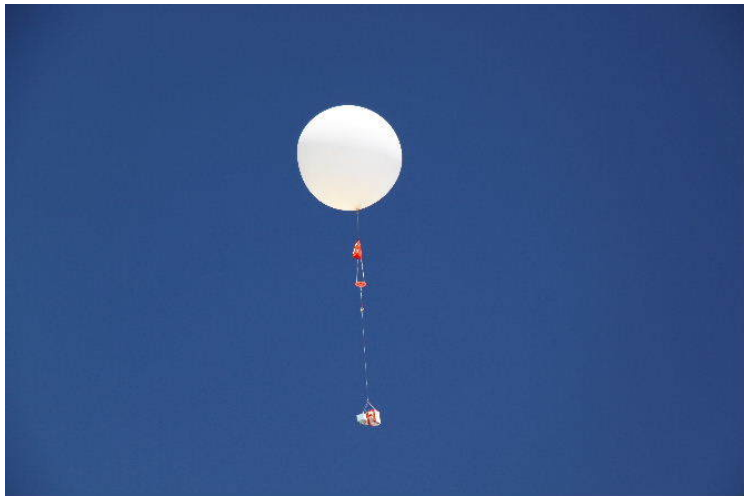

Figure 4.1: *The radiosonde package is attached to a balloon and the data are directly transmitted to the ground station through radio-frequencies (Photo credit NASA/JPL).*

as well as the country of manufacturing, that were used in this research. The oldest radiosondes use gold-beater's skin, which is a moisture-sensitive membrane made out of calf intestines. This type of sensor is still used in some Russian and Chinese sensors. The second category uses carbon hygristor and is used in most radiosondes made in the U.S. and the Chinese GTS-1 radiosonde. The carbon hygristor sensors are made of a glass or plastic strip coated with carbon particles, whose resistance varies with relative humidity. The third group belongs to the Vaisala radiosondes. These sensors are made of a dielectric material placed between two electrodes that acts as a capacitor whose capacitance changes with humidity. Some of the Russian made sensors also use a Vaisala sensor module. The last category belongs to frost point hygrometers that measure humidity based on the condensation of water vapor on a chilled mirror.

Two sensor types are of special importance and are discussed in more detail below. First, Vaisala sensors are among the most common radiosondes that are being used globally for measuring atmospheric state variables such as water vapor and temperature. Second, data from frost point hygrometers are used as the reference for calibration and bias correction of the measurements from other instruments.

4.1.1 Frost Point Hygrometer

Water vapor is condensed into moist when the temperature reaches the dew point. At very cold temperatures, water is condensed into solid ice instead of liquid water, and the temperature under which this happens in known as frost point. This forms the principle of the frost point hygrometers. A small polished

metallic mirror is electronically heated against a cryogenic cold sink to maintain a constant layer of condensate (frost) on the mirror. The thickness of the frost layer is monitored by shinning a beam of light and measuring the amount of scattered light. If the scattered light is more than expected, the mirror is too cold and need to be heated up and vice verse. This feedback loop is controlled by a microprocessor to keep the frost thickness at the desired level by continuously adjusting the temperature of the mirror. In fact, the adjustment should be very precise to be able to maintain a constant layer of frost on the mirror (NOAA, 2014; Vömel et al., 2003). The temperature of the mirror is either equal to the dew point temperature if the condensate is in liquid phase or the frost point of the ambient air if the condensate is ice. The frost point hygrometer forces the mirror to cool down to −40 °C when the measured dew point first reaches −15 °C to guaranty that the frost point temperature is measured (Miloshevich et al., 2009). The recorded dew (frost) point temperature is converted to relative humidity with respect to liquid water using Wexler (1976, 1977) vapor pressure equation, see Equation 1.9. The uncertainty (random error) in the measurements is estimated to be around 4 % of the RH values near the surface, increasing to about 9 % at the tropopause (Vömel et al., 2007a).

A schematic of the National Oceanic and Atmospheric Administration (NOAA) frost point hygrometer is shown in Figure 4.2. It should be noted that in very dry air, e.g., in stratosphere, the dew point depression can be very significant, therefore cooling system should be powerful enough to be able to control the temperature of the mirror (Vömel et al., 2003).

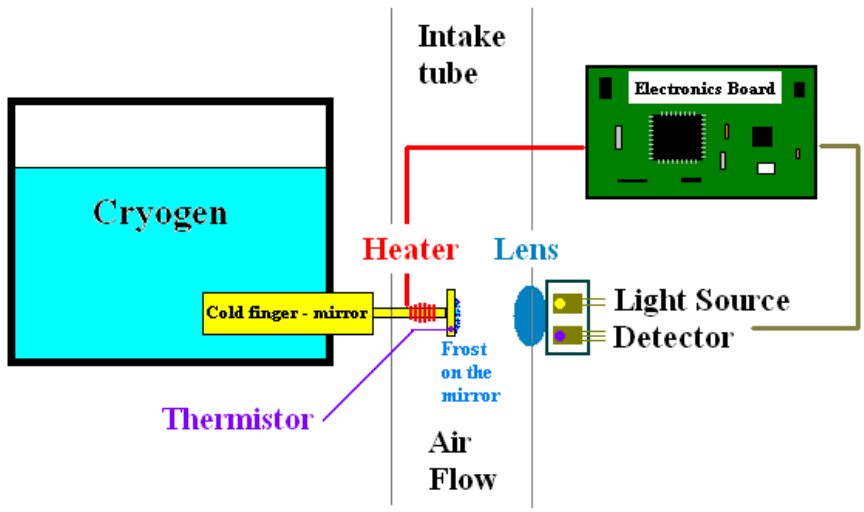

Figure 4.2: *Schematic view of the NOAA frost point hygrometer (Source: NOAA, 2014).*

4.1.2 Vaisala Humidity Sensors

Since 1980, Vaisala has been one of the largest manufactures of radiosonde sensors. The Vaisala sensors, i.e., RS80, RS90, and RS92, have been widely used for both research and operational purposes over the globe. Each of these sensors includes several subgroups that may have different characteristics in terms of errors and uncertainties. In this section, we briefly explain Vaisala sensors and related errors, since the data collected by these sensors played an important role in this research. There are four types of Vaisala radiosondes: RS80-A, RS80-H, RS90, and RS92. Both RS80 radiosondes have the same temperature sensor, but they use different humidity sensors known as A- and H-type or A- and H-Humicap, respectively. The RS80-A and RS80-H sensors were introduced around 1980 and 1993, respectively (Miloshevich et al., 2001). Both A- and H-type sensors are made of polymer, but H-type is more stable against hysteresis than the A-type polymer, especially in moist conditions (Sapucci et al., 2005). However, the time-lag error at low-temperatures, e.g., in upper-troposphere, is larger for H-type, because its response time is larger than that for A-type polymer (Miloshevich et al., 2006).

Both RS90 and RS92 sensors use the H-type polymer. The time-lag error for H-type polymers used in RS90 and RS92 is improved by using a polymer thinner than the RS80-H polymer (Miloshevich et al., 2006). In addition to the improvement of the H-type polymer, the RS90 and RS92 sensors also consist of two humidity sensors that are alternatively heated during the flight to avoid the formation of dew and ice on the sensor, especially when the radiosonde penetrates through clouds. One sensor is heated, while the other one is used for measuring the relative humidity (Miloshevich et al., 2009; Sapucci et al., 2005). Figure 4.3 shows different components of the Vaisala RS92 sensor.

Correction of Vaisala Radiosonde Data

The accuracy of the measurements of the Vaisala sensors, as well as other sensors, is affected by several factors including the absolute accuracy of the calibration, time-lag error, radiation dry bias, and a temperature-dependent bias. The last two errors are reported to be significant for some Vaisala sensors and several correction algorithms have been developed for them. Therefore, these errors are discussed in more detail in this section.

Miloshevich et al. (2001) reported that the Vaisala Humidicap-A (RS80-A) has a dry bias that is inversely correlated with the air temperature. This temperature-dependent error is introduced by using a linear approximation in the Vaisala RS80-A data processing, while the sensor response is non-linearly related to the air temperature, especially at temperatures below $-40\,^{\circ}\mathrm{C}$. Therefore, the error is not because of the limitation of the sensor, but due to the data processing algorithm (Miloshevich et al., 2001). The following polynomial equation was proposed by Miloshevich et al. (2001) for correcting the temperature-dependent error of the RS80-A sensor:

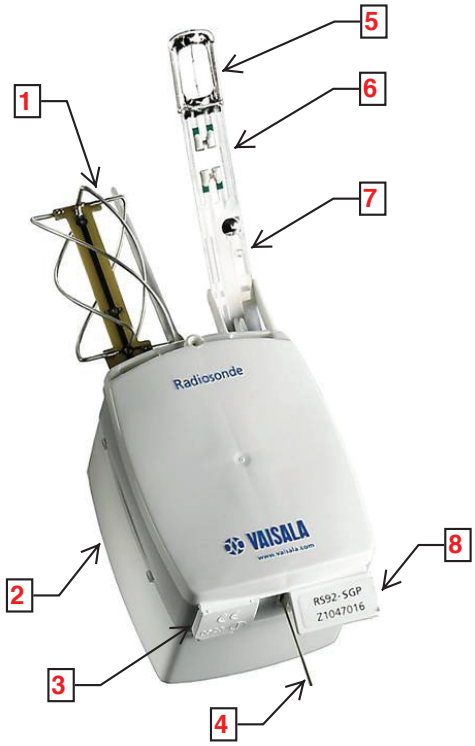

Figure 4.3: *Vaisala RS92-SGP radiosonde sensor. The numbered parts are, (1) GPS antenna, (2) Battery case, (3) Additional sensor interface connector, (4) Antenna, (5) Temperature sensor, (6) Humidity sensors, (7) Sensor boom, (8) GC25 interface (Source: www. vaisala. com).*

$$\begin{aligned} G =& 0.9278 - 5.9662 \times 10^{-3} T + 1.5783 \times 10^{-4} T^2 + \\ & 1.8179 \times 10^{-6} T^3 + 3.9407 \times 10^{-8} T^4 \end{aligned} \tag{4.1}$$

where T is temperature in celsius, and the corrected RH can be calculated as $G \times RH$. The correction term (G) is only valid in the temperature range of 0 to $-70\,^{\circ}\mathrm{C}$ and is estimated to be about $1.3\,\%$ at $-35\,^{\circ}\mathrm{C}$, $1.6\,\%$ at $-50\,^{\circ}\mathrm{C}$, and $2.4\,\%$ at $-70\,^{\circ}\mathrm{C}$. The uncertainty in the mean of corrected RH values increases from $0.06\,\%$ at $0\,^{\circ}\mathrm{C}$ to $0.11\,\%$ at $-70\,^{\circ}\mathrm{C}$ (Miloshevich et al., 2001).

Another important error in radiosonde daytime measurements is the radiation dry bias that is introduced by the exposure of the radiosonde humidity sensors to

Table 4.1: *List of radiosonde sensors with the country of manufacturing and the sensor type.*

Country	Name	Sensor type
United States	SIPPICAN 1649-540	Carbon hygristor
United States	VIZ/SIPPICAN MKIIA	Carbon hygristor
United States	VIZ/SIPPICAN B2	Carbon hygristor
Finland	VAISALA RS80A	Polymer
Finland	VAISALA RS80H	Polymer
Finland	VAISALA RS90	Polymer
Finland	VAISALA RS92	Polymer
Russia	ATTEX MTP-5H	Goldbeater's skin
Russia	MARS	Goldbeater's skin
Russia	MRZ-3A	Goldbeater's skin
Russia	AVK-RF95 VAISALA Sensors	Polymer
Russia	AVK-RF95-ARMA	Goldbeater's skin
China	Shanghai GTS1 1680 MHZ	Carbon hygristor
China	GZZ-2 403 MHZ	Goldbeater's skin

the sun (Vömel et al., 2007b). In addition, the solar heating of the temperature sensor also introduces a dry bias that is related to increase in the saturation vapor pressure. The radiation dry bias is a very significant error and has been the subject of many investigations (Sherwood, 2005; Vömel et al., 2007b; Wang et al., 2012b). RS80 sensors are equipped with a radiation shield, but RS92 sensor does not have a shield to be protected against solar radiation. Therefore, RS92 is more vulnerable to radiation dry bias than RS80. Using the data from frost point hygrometer as the reference, since the frost point hygrometer data are not affected by radiation error, Vömel et al. (2007b) developed the following correction algorithm for RS92 data:

$$C_{rad} = -0.12158 \ln P^2 + 1.664 \ln P - 4.7855 \tag{4.2}$$

where P is pressure in hPa. The corrected RH values (RH_{cor}) can be calculated using C_{rad} as well as the temperature dependent calibration correction coefficient (C_{cal}) as follows:

$$RH_{cor} = \frac{RH}{C_{rad}\, C_{cal}} \tag{4.3}$$

where C_{cal} is a temperature dependent calibration correction factor for the RS92 sensors. Table 4.2 gives the C_{cal} values at some nominal temperatures. RH values used in Equation 4.3 should be corrected for the time-lag error according to the relation proposed by Miloshevich et al. (2004). Using original RS92 measurements in Equation 4.3, causes a small degradation in relative humidity in upper

Table 4.2: *Empirical calibration correction coefficients and their uncertainties derived from RS92 nighttime data (Vömel et al., 2007b).*

T	C_{cal}	σ
0	0.98	± 0.02
-30	0.98	± 0.06
-50	0.94	± 0.03
-60	1.04	± 0.06
-70	1.13	± 0.06

troposphere (Vömel et al., 2007b). The reason for the time-lag error is that the radiosonde sensors are calibrated under steady-state conditions, while the time constant of the sensor increases exponentially with decreasing temperature. So that at cold temperatures the sensor is not able anymore to respond quickly to the changes in ambient relative humidity (Miloshevich et al., 2001)

4.1.3 Saturation Vapor Pressure Equations

Radiosonde humidity sensors are calibrated over a broad range of temperatures by the manufacturers. This range often includes very cold temperatures, lower than −40 °C, at which a bulk amount of liquid water does not exist anymore. So that the readings of the calibration equipment are based on vapor pressure over ice (e_i) which is easily measured in controlled conditions. Radiosonde measurements are conventionally reported as relative humidity over liquid even at very low temperatures, though this has little physical meaning (Miloshevich et al., 2006; Nash et al., 2010). Thus, the measurements need to be converted to relative humidity, even at super-cold temperatures, using the relation e_i/e_s, where e_s shows the saturation vapor pressure over liquid. In addition, the measurements of the frost point hygrometers are conventionally converted to vapor pressure over liquid using a similar concept (Miloshevich et al., 2006). Therefore, the saturation vapor pressure over liquid plays an important role in radiosonde measurements.

At temperatures above −40 °C, the difference among the saturation vapor pressure values over liquid calculated using different equations is negligible compared to the measurements uncertainty. Besides, all common formulations for saturation vapor pressure over ice agree with each other as well as with experimental data to better than 0.5 % over the entire atmospheric temperature range (Miloshevich et al., 2006; Nash et al., 2010). However, it is very difficult to measure vapor pressure over super cold water and almost impossible to measure vapor pressure with respect to liquid at temperatures below −40 °C, because even tiny droplets freeze immediately (Miloshevich et al., 2006). Because of the lack of experimental verification for water vapor pressure at temperatures colder than −40 °C, there is a significant difference between the water vapor equations as the definition of water vapor pressure depends on the theoretical studies (Miloshevich et al., 2006; Nash et al., 2010).

Figure 4.4 compares different equations for calculating saturation vapor pressure values over liquid at temperatures below 0 °C. As is shown and reported by Nash et al. (2010), at a temperature of −80 °C, replacing the saturation vapor pressure equation of Wexler (1977) by Bolton (1980) for performing the conversion of relative humidity over liquid to vapor pressure introduces about 15 % difference in the calculated partial pressure values. However, the most common equations for saturation water vapor pressure used by the radiosonde manufacturers, i.e., Wexler (1977), Hyland and Wexler (1983), and Sonntag (1994), yield similar results over the temperature range of interest (Nash et al., 2010). Vaisala radiosondes utilize Hyland and Wexler (1983) formulation for saturation vapor pressure over ice and Wexler (1976, 1977) for saturation vapor pressure over liquid. Note that it is straightforward to convert RH measurements to values based on a different saturation vapor pressure formulation: $RH_{new} = RH_{old} \times (e_{s,old}/e_{s,new})$ (Miloshevich et al., 2006). As long as the measurements are converted to water vapor pressure using the same equation no problem would exist. However, if the vapor pressure equation is different from what has been used by the manufacturer to calculate relative humidity, then it will introduce a systematic bias (Miloshevich et al., 2006; Nash et al., 2010).

One solution for this problem is to report relative humidity over ice at temperatures below 0 °C, since very little difference exist among the expressions for saturation vapor pressure over ice (Miloshevich et al., 2006). However, historically all radiosonde relative humidity measurements have been reported with respect to saturation vapor pressure over liquid to have a consistent definition for relative humidity at temperature below and above 0 °C. As suggested by Miloshevich et al. (2006), manufacturers can report RH with respect to both liquid and ice, and also disclose the vapor pressure equation that has been used in the calibration. This approach would allow the continuity of historical radiosonde measurements as well as provides a parameter (e_i) that can be accurately converted into other water vapor quantities.

4.2 Radiosonde Data Archives

Radiosonde data are mostly collected by operational upper air networks for weather forecasting, however, a large number of sonde data are also collected by research and reference networks such as ARM and GCOS Reference Upper Air Network (GRUAN). Data from ARM and IGRA are explained in more detail below, since these data were used in several of the papers. The ARM measurements were mainly used for validating the satellite observations, because these data are measured by high-quality Vaisala sensors and are routinely quality controlled. The IGRA data are from the operational weather stations which are measured by many different sensors, thus the quality of the data depends on the sensor type. Accordingly, a part of this research was devoted to the quantification and analysis of the errors in the IGRA humidity dataset.

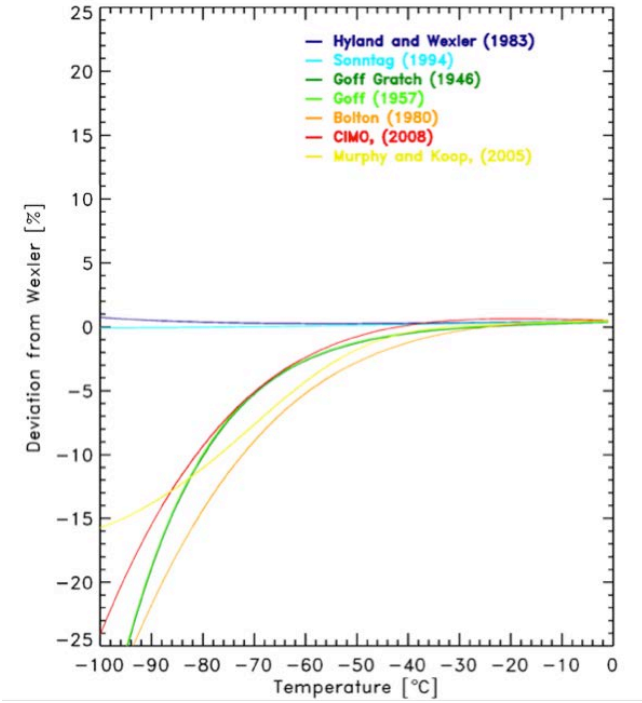

Figure 4.4: *Relative difference among some common equations for calculating water vapor pressure over liquid. The relative deviation to Wexler (1976) is shown (Source: Nash et al., 2010).*

4.2.1 ARM

The Atmospheric Radiation Measurement (ARM) Program is a global change research program supported by the U.S. Department of Energy since 1989. The primary goal of the ARM Program is to improve the understanding of the fundamental physics of the interaction between clouds and radiative feedback processes in the atmosphere. The ARM stations have been selected so that models and parameterization can be tested over a broad range of conditions to give confidence in their general applicability (Stokes and Schwartz, 1994). The ARM radiosonde dataset includes moisture, pressure, temperature, and wind profiles.

Radiosonde data from the Tropical Western Pacific (TWP-C1, -C2, and -C3) and Southern Great Plains (SGP-C1) stations were used in the current research. These stations are located at Manus, Nauru Island, Darwin, and Lamont Oklahoma, respectively, see Figure 4.5. The TWP stations, especially TWP-C1 and TWP-C2, are particularly close to the equator and are located in a tropical convective zone. TWP-C1 is also located in the tropical region, but in a relatively dry region. SGP-C1 is a mid-latitude station located in a temperate region in

the South Central United States.

4.2.2 IGRA

The Integrated Global Radiosonde Archive (IGRA) project, operated by the NOAA's National Climatic Data Center (NCDC), consists of radiosonde observations from around the world. According to Durre et al. (2006), 65 % to 75 % of the IGRA profiles reach 100 hPa, but just 20 % to 30 % reach 10 hPa, see Figure 8 in Durre et al. (2006). Since 1958, the most frequent observation times at IGRA stations are 00:00 and 12:00 UTC, and most stations have two launches per day (Durre et al., 2006). The dataset consists of data from over 1500 globally distributed stations. The geographic distribution of IGRA stations as well as the period of the availability of the data are shown in Figure 4.5.

Operational radiosonde data are normally reported at mandatory and significant pressure levels. Mandatory levels, also known as standard levels, are pressure levels determined by World Meteorological Organization (WMO) where the atmospheric state variables should be reported, if available. These levels are, the surface, 1000, 925, 850, 700, 500, 400, 300, 250, 200, 150, 100, 70, 50, and 10 hPa. Significant levels indicate the points where a significant change in temperature or humidity is detected. Radiosonde profiles can be reproduced using significant and mandatory levels by assuming that temperature and water vapor change linearly with height between the significant levels. The interpolation can only be properly performed if the significant levels are reported. Therefor, in this research, we only used the IGRA profiles that had both mandatory and significant levels.

It should be noted that operational networks normally launch radiosondes about 30 min before the synoptic time. For instance, if the synoptic date/time is 24:00 UTC January 10, 2014, then the radiosonde launch time would be 23:30 UTC January 9, 2014. The IGRA dataset reports the date only for the actual synoptic time (in this case January 10, 2014), but the time is reported for both radiosonde launch time and synoptic time. Thus, the synoptic date should be reduced by one day if it is used in conjunction with the radiosonde launch time at 23:30 UTC. This issue does not exist for 12:00 UTC launches, since the radiosonde launch date and the synoptic date are the same.

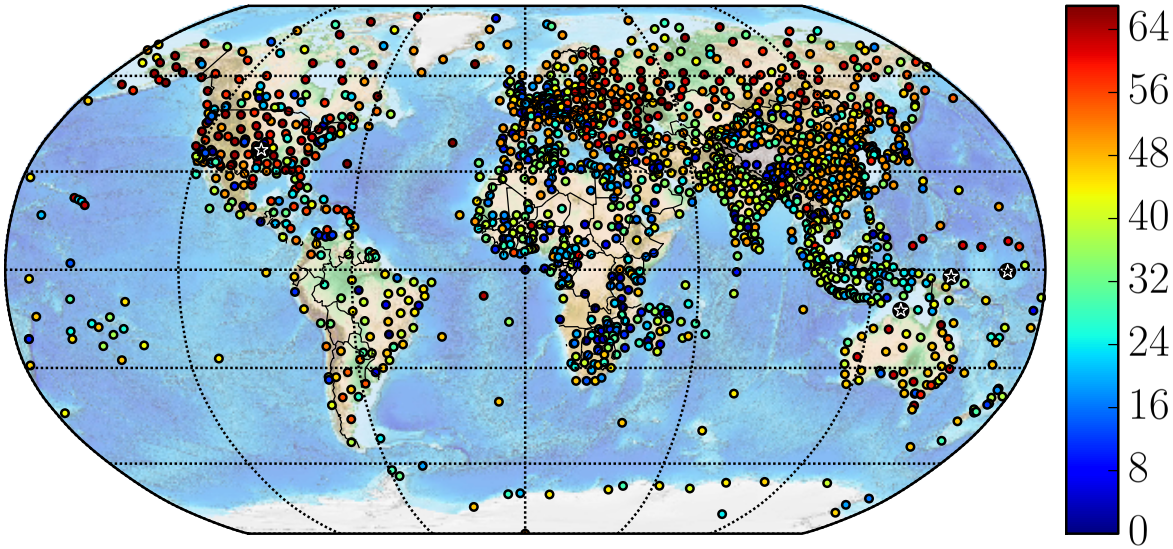

Figure 4.5: *Distribution of IGRA and ARM stations. The colorbar indicates the length of the time period of the data, in years. The white-star symbols show the location of the ARM stations.*

5

Conclusions and Outlook

This chapter gives an overview of the dissertation, the papers that were published as part of the Ph.D. research, as well as an outlook for future research.

5.1 Summary and Findings

Water vapor directly and indirectly influences the Earth's climate. However, despite the importance of water vapor, there is a lack of accurate long-term observations for climate and weather studies. The ultimate goal of the dissertation was to develop advanced techniques that are required for developing long-term tropospheric humidity data records, known as ESDR or CDR, from microwave satellite and radiosonde data. Therefore, papers published mainly focus on developing advanced correction and homogenization techniques for microwave satellite observations and radiosonde data. Although, many of the correction techniques developed in this research are primarily for water vapor measurements, they can be directly or indirectly used for developing CDR for other geophysical variables such as air temperature. Further, since satellite remote sensing observations are indirect measurements and need to be transformed into desired variables, a part of the thesis focused on developing algorithms to retrieve tropospheric humidity from microwave satellite observations.

Paper I evaluates the accuracy of microwave satellite observations using high-quality radiosonde data from the ARM Program. Paper II introduces an advanced technique for correcting the geolocation errors in microwave satellite data, Paper III investigates and quantifies errors and uncertainties in the operational radiosonde data, Paper IV introduces a technique to derive layer-averaged tropospheric humidity from microwave observations, and Paper V validates ATMS and SAPHIR observations by inter-comparing observations from the two instruments as well as validating against in-situ radiosonde and Global Positioning

System - Radio Occultation (GPS-RO) data.

The main findings of this research are listed in the following and more information about these findings is available in the papers:

- ARM radiosonde data provide a great opportunity for validating microwave satellite observations, especially as several of the ARM stations are located on small islands which helps to avoid emissivity issues for the radiative transfer calculations. However, there are still several important errors in the radiosonde humidity measurements which are related to the sensors. Therefore, more accurate humidity sensors are required for better validation of the microwave water vapor channels.
- Satellite microwave channels that are sensitive to the surface can not still be validated because of the lack of accurate surface emissivity data. Thus, alternative methods must be found for validating these channels.
- Geolocation errors in microwave satellite data can significantly affect the quality of the data especially over inhomogeneous regions or cloudy areas.
- Most of the operational radiosonde data are not suitable for climate studies and only a few operational stations may provide long-term quality data for climate studies. Operational radiosonde data need to be extensively evaluated and be homogenized for climate applications. Yet, it may not be possible to correct the operational radiosonde data that have large biases with sufficient accuracy for climate applications.
- Microwave satellite sensors generally have good accuracy in the beginning of the mission, however the quality of the data degrades with time. Therefore, permanent monitoring of the microwave satellite observations is required.
- More than 15 years of data are now available from microwave humidity sounders that can be used for developing long-term CDRs of tropospheric humidity. Such a dataset is under development that will serve as a great database for weather and climate applications.

5.2 Appended Papers

A summary of the papers that are appended to this dissertation is given here. Related papers directly contribute to the thesis, but they are neither appended nor discussed here.

Paper I

Satellite data from cross-track microwave humidity sounders, e.g., AMSU-B and MHS, are a valuable source of information for UTH. These data have global coverage and are available from late 1998 to present, so provide one of the longest records of UTH with global coverage. These measurements are assimilated into Numerical Weather Prediction (NWP) models, and are also utilized

for may other weather and climate applications, including validating the simulations of UTH by weather and climate prediction models, and investigating the water vapor feedback in the climate system. However, microwave satellite data are subject to errors and uncertainties. Thus, these observations need to be extensively validated especially before being used for developing long-term CDRs. Brightness temperatures simulated using radiosonde data and a radiative transfer model provide a valuable tool for evaluating microwave satellite observations. However, radiosonde data should have sufficient accuracy to be able to serve as the reference. Radiosonde data from ARM have already been extensively validated through inter-comparison with measurements from reference sensors such as frost-point hygrometers. These inter-comparisons have reported a small dry bias in mid-upper troposphere during nighttime, but a relatively larger bias known as the radiation dry bias during daytime for ARM data. This paper compares the AMSU-B and MHS measurements against radiosonde data measured at four of the central facilities of the ARM program. The Atmospheric Radiative Transfer Simulator (ARTS) was used to simulate satellite brightness temperatures from the radiosonde profiles. After proper matching of simulated and observed measurements, a good agreement was found between the two datasets. Then, a simple transformation technique was used to transform both observed and simulated brightness temperatures to UTH. The comparison between the UTH values showed that the values retrieved from satellite measurements were slightly moister than the values retrieved from simulated brightness temperatures, with a mean difference of 1 %RH to 2.3 %RH, depending on the radiosonde site.

Paper II

Geolocation errors are a significant source of uncertainty in the microwave satellite measurements. These errors are caused by several factors, such as instrument misalignment, satellite clock offset, and sensor modeling error. Correcting geolocation errors is one of the main requirements for developing long-term CDRs from microwave satellite data. Correcting geolocation errors is also an important step in utilizing satellite data for other applications such as assimilating cloud contaminated data into NWP models or retrieving geophysical variables from satellite data. Currently, no geolocation correction is performed on data from microwave instruments onboard the satellites in the NOAA Polar Operational Environmental Satellite (POES) program. Because of the coarse spatial resolution of microwave satellite data, the accuracy of the geolocation of microwave satellite data cannot be simply evaluated using coastline checks. This paper investigated and corrected the geolocation errors of the observations from AMSU-A onboard NOAA-15 to -19, AMSU-B onboard NOAA-15 to -17, and MHS onboard NOAA-18, and -19. The difference between ascending and descending observations along the coastlines was used to quantify the geolocation errors in terms of the satellite attitudes (Euler angles), i.e., pitch, roll, and yaw. The results showed that NOAA-15 AMSU-A2 sensor is mounted about 1.2° positive cross-track, and about 0.5° negative along-track. NOAA-16 AMSU-A1 and

-A2 are mounted about 0.5° negative alongtrack, and NOAA-18 AMSU-A2 is mounted more than 1° negative alongtrack. A new geolocation dataset, i.e., Earth location of the measurements, scan angle, and Earth incidence angle, was developed using new attitudes as part of this research that will be delivered to NCDC for distribution.

Paper III

Radiosondes are the only instruments that are used globally to directly measure the vertical distribution of tropospheric humidity. Among radiosonde measurements, global operational radiosonde data provide the largest source of direct measurement of tropospheric humidity. However, operational radiosonde data are measured by a variety of different instruments that have different systematic and random errors. This introduces temporal and spatial inhomogeneity in the operational radiosonde data. So that, operational radiosonde data do not meet the requirements for climate assessments. The first step in developing a long-term data record from radiosonde data is to properly quantify these errors. This paper evaluated the quality of humidity measurements from global operational radiosonde sensors in upper-, middle-, and lower-troposphere for the period 2000-2011 using satellite observations from three microwave water vapor channels operating at 183.31±1, 183.31±3, and 183.31±7 GHz. Radiosonde data were partitioned based on sensor type into 19 classes. The satellite brightness temperatures (Tb) were simulated using radiosonde profiles and a radiative transfer model, then the radiosonde simulated Tb's were compared with the satellite observed Tb's. Daytime and nighttime data were examined separately to investigate the possible effect of daytime radiation bias on the radiosonde data. The error characteristics significantly vary among the instruments and the differences are more evident in middle- and upper-troposphere than in the lower-troposphere. Some of the sensors have large systematic and random errors in the upper-troposphere, because these sensors stop responding to tropospheric humidity at cold temperatures. The results clearly indicate that most of the data from the current operational radiosonde networks are not suitable for long-term climate studies, unless the data are measured using a single type of sensor at any given station.

Paper IV

Satellite microwave humidity sounders provide indirect measurements of tropospheric humidity in terms of radiance or brightness temperature. However, most climate applications require water vapor measurements. Therefore, inversion or transformation techniques are required to derive atmospheric water vapor from satellite measurements. These techniques can be classified into full inversion and simple transformation methods. Full inversion techniques are able to retrieve humidity profiles from satellite measurements. Since the current microwave instruments only offer a few water vapor channels, the full inversion techniques do not perform satisfactory using these measurements as input. Besides, the full inversion techniques are computationally expensive as well as require a-

priori information and error covariance matrices to derive the vertical profiles of geophysical variables. ATMS, as the newest generation of microwave sounders onboard polar orbiting satellites, provides information on tropospheric humidity in different layers. ATMS is currently flying on S-NPP and is also planned to fly on the next generation of the U.S. polar orbiting satellites named JPSS. This paper presents a simple method to directly transform observations from ATMS water vapor channels into layer-averaged tropospheric humidity (LAH). The method is based on a linear relation between the ATMS measurements and natural logarithm of Jacobian weighted tropospheric humidity. The empirical coefficients are presented for all ATMS water vapor channels that can be used in conjunction with the ATMS data to derive LAH for upper to lower-troposphere. An extensive validation using independent datasets showed that the bias for the transformation method is less than 10 % in most cases. In addition, the method was validated using collocated ATMS measurements and humidity profiles from the European Center for Medium range Weather Forecasting (ECMWF) Interim Reanalysis (ERA-interim). In this case, the bias did not indicate any significant regional dependency when actual Jacobians were used to calculate LAH.

Paper V

ATMS onboard S-NPP and SAPHIR onboard M-T are the most recent spaceborne microwave sounders that provide information about tropospheric water vapor on a global scale and in the tropical region, respectively. Post-launch evaluation of the radiometric accuracy of these microwave observations is necessary for both weather and climate applications. In the lack of reference datasets identical to satellite observations (same geometry and same physical value), several alternative methods can be used for post-launch evaluation of the microwave satellite observations. This paper employs several of these methods, including (i) data simulated using radiosonde profiles to evaluate the water vapor channels as well as temperature sounding channels sensitive to middle and upper troposphere, (ii) simulated data using GPS-RO observations to evaluate the temperature sounding channels sensitive to upper troposphere and lower stratosphere, and (iii) inter-comparing ATMS and SAPHIR data from similar channels. Since SAPHIR and ATMS channels operate at slightly different frequencies, radiative transfer simulations were performed to quantify the impact of the frequency difference on the inter-comparison results. The bias due to radiometric errors was calculated as the difference between observed and simulated differences between the two instruments. This difference that is often referred to as double difference ranges between 0.3 K to 0.7 K which shows a good consistency between the ATMS and SAPHIR instruments. The difference between radiosonde simulated and observed values for the ATMS temperature sounding channels was less than 0.5 K at most stations. However, the difference between the observed values from ATMS/SAPHIR water vapor channels and radiosonde simulated values was larger (0.5 K to 2.0 K) which is mainly due to error in radiosonde humidity profiles. The difference between GPS-RO simulated and observed values was less than 0.4 K for the ATMS Channels 10-14. Overall, the results show that

both ATMS and SAPHIR have good accuracy with a radiometric error less than pre-launch specifications.

5.3 Outlook

Radiosonde data from ARM Program provide a valuable dataset for validating satellite observations from microwave water vapor channels, however the data still suffer from several biases, such as daytime radiation dry bias. Since these biases are introduced by radiosonde humidity sensors, more accurate radiosonde sensors are required for validating microwave satellite observation with a higher confidency. In recent years, GRUAN has focused on quantifying errors and uncertainties in the radiosonde observations (Dirksen et al., 2014). This practice is very helpful for quantifying and documenting the uncertainties, but GRUAN is still using the same radiosonde sensors as ARM program. Vaisala has recently developed a new sensor named RS42 which may help to overcome some of these issues.

The quality of the operational radiosonde data was investigated in this research, however more research work is required to homogenize operational radiosonde humidity data. Several studies have previously focused on the homogenization of radiosonde temperature data, e.g., Haimberger (2007) and Lanzante et al. (2003), but there has been only a limited effort for the homogenization of radiosonde humidity data, mainly using statistical methods trying to self-homogenize the time series (Dai et al., 2011). These statistical methods largely rely on the recent years of observation as the truth, but as it has been discussed in the appended papers, in some cases historical data may have better quality than recent data. Satellite CDRss provide a great opportunity for homogenization of radiosonde humidity data but extensive work is required to achieve this.

This research used the difference between Tb's from upper and lower microwave channels to identify cloud contaminated data. This method is sufficient to flag the cloudy radiances in the presence of convective clouds, but it my not be able to detect the thin clouds that have a small influence on the radiances. This introduces a systematic error in the comparisons in the presence of thin clouds, because cloud contaminated Tb's are systematically lower than clear-sky Tb's. Thus, more research is required on the cloud filter and its validation under different conditions.

Routine calibration and validation of satellite observations should consider monitoring geolocation errors. The method presented in this dissertation, provides a valuable tool for monitoring and correcting the geolocation errors for microwave observations. However, this technique can not be used for observations that are not sensitive to the surface or for observations from low-inclination satellites. More work is required to extend this technique to other satellites or channels that are not sensitive to the surface. Geolocation can significantly affect cloudy radiances or observations over inhomogeneous surfaces, therefore it is required to evaluate the impact of geolocation errors on the assimilation of microwave

cloudy radiances or observations over inhomogeneous surfaces.

Polar-orbiting and low-inclination satellites are not synchronized, thus observations from low-inclination satellites, e.g., the M-T satellite, provide frequent coincident observations especially in the tropical region. These coincident observations provide a great opportunity for monitoring the quality of observations from polar-orbiting satellites. In addition, these coincident observations can be used as transfer function to inter-calibrate observations from polar-orbiting satellites.

Bibliography

Ahrens, C.D. *Meteorology Today: An Introduction to Weather, Climate, and the Environment*. Thomson/Brooks/Cole, Belmont, CA, 2007. ISBN 0495011622.

Baars, J.W.M. *The Paraboloidal Reflector Antenna in Radio Astronomy and Communication: 348*. Springer New York, 2007.

Baker, N. Advanced Technology Microwave Sounder (ATMS). SDR radiometric calibration. Algorithm Theoretical Basis Document (ATBD). Joint Polar Satellite System (JPSS) Ground Project, 2011. URL http://npp.gsfc.nasa.gov/sciencedocuments/ATBD_122011/474-00043_Rev-Baseline.pdf.

Berry, H.G., Gabrielse, G. and Livingston, A.E. Measurement of the Stokes parameters of light. *Appl. Opt.*, 16(12):3200–3205, 1977. doi: 10.1364/AO.16.003200.

Betts, A.K. and Ridgway, W. Coupling of the radiative, convective, and surface fluxes over the equatorial pacific. *J. Atmos. Sci.*, 45(3):522–536, 1988. doi: 10.1175/1520-0469(1988)045⟨0522:COTRCA⟩2.0.CO;2.

Bolton, D. The computation of equivalent potential temperature. *Mon. Wea. Rev.*, 108(7):1046–1053, 1980. doi: 10.1175/1520-0493(1980)108⟨1046:TCOEPT⟩2.0.CO;2.

Buehler, S.A. and John, V.O. A simple method to relate microwave radiances to upper tropospheric humidity. *J. Geophys. Res.*, 110(D2):D02110, 2005. doi: 10.1029/2004JD005111.

Buehler, S.A. et al. ARTS, the atmospheric radiative transfer simulator. *J. Quant. Spectrosc. Radiat. Transf.*, 91(1):65–93, 2005. doi: 10.1016/j.jqsrt.2004.05.051.

Cess, R.D. et al. Intercomparison and interpretation of climate feedback processes in 19 atmospheric general circulation models. *J. Geophys. Res.*, 95 (D10):16601–16615, 1990. doi: 10.1029/JD095iD10p16601.

Chandrasekhar, S. *Radiative Transfer*. Dover Publications, New York, 2011. ISBN 9780486605906.

Chung, E.S. et al. Model-simulated humidity bias in the upper troposphere and its relation to the large-scale circulation. *J. Geophys. Res.*, 116:14 PP., 2011. doi: 201110.1029/2011JD015609.

Dai, A. et al. A new approach to homogenize daily radiosonde humidity data. *J. Clim.*, 24(4):965–991, 2011. doi: 10.1175/2010JCLI3816.1.

Dessler, A.E. and Sherwood, S.C. Atmospheric science: A matter of humidity. *Sci.*, 323(5917):1020–1021, 2009. doi: 10.1126/science.1171264.

Dirksen, R.J. et al. Reference quality upper-air measurements: GRUAN data processing for the Vaisala RS92 radiosonde. *Atmos. Meas. Tech. Discuss.*, 7 (4):3727–3800, 2014. doi: 10.5194/amtd-7-3727-2014.

Durre, I., Vose, R.S. and Wuertz, D.B. Overview of the integrated global radiosonde archive. *J. Clim.*, 19(1):53–68, 2006. doi: 10.1175/JCLI3594.1.

Elliott, W.P. and Gaffen, D.J. On the utility of radiosonde humidity archives for climate studies. *Bull. Am. Meteorol. Soc.*, 72(10):1507–1520, 1991. doi: 10.1175/1520-0477(1991)072⟨1507:OTUORH⟩2.0.CO;2.

Eriksson, P. et al. ARTS, the atmospheric radiative transfer simulator, version 2. *J. Quant. Spectrosc. Radiat. Transf.*, 112(10):1551–1558, 2011. doi: 10.1016/j.jqsrt.2011.03.001.

Garand, L. et al. Radiance and jacobian intercomparison of radiative transfer models applied to HIRS and AMSU channels. *J. Geophys. Res.*, 106(D20): 24017–24,031, 2001. doi: 10.1029/2000JD000184.

Goodrum, G., Kidwell, K.B. and Winston, W. NOAA KLM user's guide. Technical report, National Environmental Satellite, Data, and Information Services (NESDIS), 2007.

Goody, R.M. and Yung, Y.L. *Atmospheric Radiation: Theoretical Basis*. Oxford University Press, New York, 1989. ISBN 9780195051346.

Haimberger, L. Homogenization of radiosonde temperature time series using innovation statistics. *J. Clim.*, 20(7):1377–1403, 2007. doi: 10.1175/JCLI4050.1.

Held, I.M. and Soden, B.J. Water vapor feedback and global warming. *Annu. Rev. Energy Environ.*, 25(1):441–475, 2000. doi: 10.1146/annurev.energy.25.1.441.

Held, I.M. and Soden, B.J. Robust responses of the hydrological cycle to global warming. *J. Clim.*, 19(21):5686–5699, 2006. doi: 10.1175/JCLI3990.1.

Hewison, T. and Saunders, R. Measurements of the AMSU-B antenna pattern. *IEEE Transactions on Geosci. Remote. Sens.*, 34(2):405–412, 1996. doi: 10.1109/36.485118.

Hyland, W. and Wexler, A. Formulations for the thermodynamic properties of the saturated phases of H_2O from 173.15 k to 473.15 k. *ASHRAE Transactions*, 89(2A):500–519, 1983.

Janssen, M.A. *Atmospheric Remote Sensing by Microwave Radiometry.* John Wiley & Sons, 1993. ISBN 0471628913.

Jones, A.S. and Vonder Haar, T.H. Retrieval of microwave surface emittance over land using coincident microwave and infrared satellite measurements. *J. Geophys. Res.*, 102(D12):13609–13626, 1997. doi: 10.1029/97JD00797.

Karbou, F. and Prigent, C. Calculation of microwave land surface emissivity from satellite observations: validity of the specular approximation over snow-free surfaces? *IEEE Geosci. Remote. Sens. Lett.*, 2(3):311–314, 2005. doi: 10.1109/LGRS.2005.847932.

Karbou, F., Gérard, E. and Rabier, F. Microwave land emissivity and skin temperature for AMSU-A and -B assimilation over land. *Q.J.R. Meteorol. Soc.*, 132(620):2333–2355, 2006. doi: 10.1256/qj.05.216.

Kaviany, M. *Principles of Heat Transfer.* Wiley-Interscience, New York, 2001. ISBN 9780471434634.

Keil, C. et al. Sensitivity of quantitative precipitation forecast to height dependent changes in humidity. *Geophys. Res. Lett.*, 35(9):L09812, 2008. doi: 10.1029/2008GL033657.

Kim, E. et al. S-NPP ATMS instrument prelaunch and on-orbit performance evaluation. *J. Geophys. Res. Atmos.*, 119(9):2013JD020483, 2014. doi: 10.1002/2013JD020483.

Klein, L. and Swift, C. An improved model for the dielectric constant of sea water at microwave frequencies. *IEEE Transactions on Antennas Propag.*, 25 (1):104–111, 1977. doi: 10.1109/TAP.1977.1141539.

Kuntz, M. and Höpfner, M. Efficient line-by-line calculation of absorption coefficients. *J. Quant. Spectrosc. Radiat. Transf.*, 63(1):97–114, 1999. doi: 10.1016/S0022-4073(98)00140-X.

Lanzante, J.R., Klein, S.A. and Seidel, D.J. Temporal homogenization of monthly radiosonde temperature data. part i: Methodology. *J. Clim.*, 16(2): 224–240, 2003. doi: 10.1175/1520-0442(2003)016⟨0224:THOMRT⟩2.0.CO;2.

Liou, K.N. *An Introduction to Atmospheric Radiation.* Academic Press, Amsterdam ; Boston, 2002. ISBN 9780124514515.

Matzler, C. On the determination of surface emissivity from satellite observations. *IEEE Geosci. Remote. Sens. Lett.*, 2(2):160–163, 2005. doi: 10.1109/LGRS.2004.842448.

Meissner, T. and Wentz, F. The complex dielectric constant of pure and sea water from microwave satellite observations. *IEEE Transactions on Geosci. Remote. Sens.*, 42(9):1836–1849, 2004. doi: 10.1109/TGRS.2004.831888.

Meissner, T. and Wentz, F. The emissivity of the ocean surface between 6 and 90 GHz over a large range of wind speeds and earth incidence angles. *IEEE Transactions on Geosci. Remote. Sens.*, 50(8):3004–3026, 2012. doi: 10.1109/TGRS.2011.2179662.

Miloshevich, L. et al. Absolute accuracy of water vapor measurements from six operational radiosonde types launched during AWEX-G and implications for AIRS validation. *J. Geophys. Res.*, 111(D9), 2006.

Miloshevich, L.M. et al. Characterization and correction of relative humidity measurements from Vaisala RS80-A radiosondes at cold temperatures. *J. Atmospheric & Ocean. Technol.*, 18(2):135, 2001.

Miloshevich, L.M. et al. Accuracy assessment and correction of vaisala RS92 radiosonde water vapor measurements. *J. Geophys. Res.*, 114(D11), 2009. doi: 10.1029/2008JD011565.

Miloshevich, L. et al. Development and validation of a time-lag correction for Vaisala radiosonde humidity measurements. *J. Atmospheric Ocean. Technol.*, 21(9):1305–1327, 2004. doi: 10.1175/1520-0426(2004)021⟨1305:DAVOAT⟩2.0.CO;2.

Minschwaner, K. and Dessler, A.E. Water vapor feedback in the tropical upper troposphere: Model results and observations. *J. Clim.*, 17(6):1272–1282, 2004. doi: 10.1175/1520-0442(2004)017⟨1272:WVFITT⟩2.0.CO;2.

Mishchenko, M.I., Hovenier, J.W. and Travis, L.D., editors. *Light Scattering by Nonspherical Particles: Theory, Measurements, and Applications.* Academic Press, San Diego, 1999. ISBN 9780124986602.

Mo, T. Prelaunch calibration of the advanced microwave sounding unit-a for NOAA-k. *IEEE Transactions on Microw. Theory Tech.*, 44(8):1460–1469, 1996. doi: 10.1109/22.536029.

Moradi, I. et al. Assessing the quality of humidity measurements from global operational radiosonde sensors. *J. Geophys. Res. Atmos.*, 118(14):8040–8053, 2013. doi: 10.1002/jgrd.50589.

Nash, J. et al. WMO intercomparison of high quality radiosonde systems. Technical report, World Meteorological Organization, Yangjiang, China, 2010.

National Research Council (U.S.). *Climate data records from environmental satellites*. National Academies Press, Washington, D.C, 2004. ISBN 0309091683.

NOAA, N.W.S. NOAA national weather service radiosonde observations, 2014.

Okamoto, K., editor. *Global Environment Remote Sensing*. Ios Pr Inc, Chiyoda-ku, Tokyo : Burke, Va, 2000. ISBN 9781586031015.

Peach, G. Theory of the pressure broadening and shift of spectral lines. *Adv. Phys.*, 30(3):367–474, 1981. doi: 10.1080/00018738100101467.

Pierrehumbert, R.T., Brogniez, H. and Roca, R. On the relative humidity of the atmosphere. In Schneider, T. and Sobel, A., editors, *The Global Circulation of the Atmosphere*. Princeton University Press, Princeton, N.J, 2007. ISBN 9780691121819.

Prigent, C., Rossow, W.B. and Matthews, E. Microwave land surface emissivities estimated from SSM/I observations. *J. Geophys. Res.*, 102(D18): 21867–21890, 1997. doi: 10.1029/97JD01360.

Radmanesh, P.D.M.M. *Advanced RF & Microwave Circuit Design: The Ultimate Guide to Superior Design*. AuthorHouse, 2009. ISBN 9781425972448.

Randel, D.L. et al. A new global water vapor dataset. *Bull. Am. Meteorol. Soc.*, 77(6):1233–1246, 1996. doi: 10.1175/1520-0477(1996)077⟨1233:ANGWVD⟩2.0.CO;2.

Rodgers, C.D. *Inverse Methods for Atmospheric Sounding: Theory and Practice*. World Scientific Publishing, 2000. ISBN 9789810227401.

Rogers, R.R. and Yau, M.K. *A Short Course in Cloud Physics*. Butterworth-Heinemann, 1989. ISBN 9780750632157.

Rothman, L.S. et al. The HITRAN 2008 molecular spectroscopic database. *J. Quant. Spectrosc. Radiat. Transf.*, 110(9–10):533–572, 2009. doi: 10.1016/j.jqsrt.2009.02.013.

Russer, P. *Electromagnetics, Microwave Circuit and Antenna Design for Communications Engineering*. Artech House, 2003. ISBN 9781580535328.

Salvia, V.K. *Antenna and Wave Propagation*. Laxmi Publications, 2007. ISBN 9788131805411.

Sapucci, L.F. et al. Analysis of relative humidity sensors at the WMO radiosonde intercomparison experiment in Brazil. *J. Atmospheric Ocean. Technol.*, 22(6):664–678, 2005. doi: 10.1175/JTECH1754.1.

Sharkov, E.A. *Passive Microwave Remote Sensing of the Earth: Physical Foundations*. Springer, Berlin ; New York : Chichester, UK, 2003. ISBN 9783540439462.

Sherwood, S.C. Radiosonde daytime biases and late-20th century warming. *Sci.*, 309(5740):1556–1559, 2005. doi: 10.1126/science.1115640.

Sherwood, S.C. Direct versus indirect effects of tropospheric humidity changes on the hydrologic cycle. *Environ. Res. Lett.*, 5(2):025206, 2010. doi: 10.1088/1748-9326/5/2/025206.

Sherwood, S.C. et al. Tropospheric water vapor, convection, and climate. *Rev. Geophys.*, 48(2):RG2001, 2010. doi: 10.1029/2009RG000301.

Sherwood, S.C., Kursinski, E.R. and Read, W.G. A distribution law for free-tropospheric relative humidity. *J. Clim.*, 19(24):6267–6277, 2006. doi: 10.1175/JCLI3978.1.

Shine, K.P. and Sinha, A. Sensitivity of the earth's climate to height-dependent changes in the water vapour mixing ratio. *Nat.*, 354(6352): 382–384, 1991. doi: 10.1038/354382a0.

Siegel, R. *Thermal Radiation Heat Transfer*. Taylor & Francis, New York, 2001. ISBN 9781560328391.

Soden, B.J. et al. The radiative signature of upper tropospheric moistening. *Sci.*, 310(5749):841–844, 2005. doi: 10.1126/science.1115602.

Soden, B.J. and Bretherton, F.P. Upper tropospheric relative humidity from the GOES 6.7 μm channel: Method and climatology for July 1987. *J. Geophys. Res.*, 98(D9):16669–16688, 1993. doi: 10.1029/93JD01283.

Sonntag, D. Advancements in the field of hygrometry. *Meteorol. Z.*, 3(1):51–66, 1994.

Spencer, R.W. and Braswell, W.D. How dry is the tropical free troposphere? implications for global warming theory. *Bull. Amer. Meteor. Soc.*, 78(6): 1097–1106, 1997. doi: 10.1175/1520-0477(1997)078⟨1097:HDITTF⟩2.0.CO;2.

Stokes, G.M. and Schwartz, S.E. The atmospheric radiation measurement (ARM) program: Programmatic background and design of the cloud and radiation test bed. *Bull. Amer. Meteor. Soc.*, 75(7):1201–1221, 1994. doi: 10.1175/1520-0477(1994)075⟨1201:TARMPP⟩2.0.CO;2.

Team, M.T. Megha-Tropiques level 1 products definition. Centre National d'Etudes Spatiales (CNES), 2013. URL http://meghatropiques.ipsl.polytechnique.fr.

Thomas, G.E. and Stamnes, K. *Radiative Transfer in the Atmosphere and Ocean*. Cambridge University Press, Cambridge; New York, 2002. ISBN 9780521890618.

Thorne, A., Litzén, U. and Johansson, S. *Spectrophysics: Principles and Applications*. Springer Science & Business Media, 1999. ISBN 9783540651178.

Trenberth, K.E., Fasullo, J.T. and Kiehl, J. Earth's global energy budget. *Bull. Am. Meteorol. Soc.*, 90(3):311–323, 2009. doi: 10.1175/2008BAMS2634.1.

Vömel, H. et al. The behavior of the snow white chilled-mirror hygrometer in extremely dry conditions. *J. Atmos. Ocean. Technol.*, 20(11):1560–1567, 2003. doi: 10.1175/1520-0426(2003)020⟨1560:TBOTSW⟩2.0.CO;2.

Vömel, H., David, D.E. and Smith, K. Accuracy of tropospheric and stratospheric water vapor measurements by the cryogenic frost point hygrometer: Instrumental details and observations. *J. Geophys. Res.*, 112 (D8), 2007a. doi: 10.1029/2006JD007224.

Vömel, H. et al. Radiation dry bias of the vaisala RS92 humidity sensor. *J. Atmospheric Ocean. Technol.*, 24(6):953–963, 2007b. doi: 10.1175/JTECH2019.1.

Wang, C. et al. Retrieval of ice cloud properties from AIRS and MODIS observations based on a fast high-spectral-resolution radiative transfer model. *J. Appl. Meteor. Clim.*, 52(3):710–726, 2012a. doi: 10.1175/JAMC-D-12-020.1.

Wang, J. et al. Radiation dry bias correction of vaisala RS92 humidity data and its impacts on historical radiosonde data. *J. Atmos. Ocean. Technol.*, 30 (2):197–214, 2012b. doi: 10.1175/JTECH-D-12-00113.1.

Weng, F. and Zou, X. Errors from Rayleigh-Jeans approximation in satellite microwave radiometer calibration systems. *Appl Opt*, 52(3):505–508, 2013.

Weng, F., Yang, H. and Zou, X. On convertibility from antenna to sensor brightness temperature for ATMS. *IEEE Geosci. Remote. Sens. Lett.*, 10(4): 771–775, 2013. doi: 10.1109/LGRS.2012.2223193.

Wexler, A. Vapor pressure formulation for water in range 0 to 100 ^{o}C. a revision. *J. Res. Natl. Bur. Stand.*, 80:775–785, 1976.

Wexler, A. Vapor pressure formulation for ice. *J. Res. Natl. Bureau Standards*, 81A(1):5–20, 1977.

Woodhouse, I.H. *Introduction to Microwave Remote Sensing*. CRC Press, Boca Raton, 2005. ISBN 9780415271233.